EFFECTS OF SPATIAL ENERGY DISTRIBUTION-INDUCED POROSITY ON MECHANICAL PROPERTIES OF LASER POWDER BED FUSION 316L STAINLESS STEEL

A Dissertation
Presented to
The Academic Faculty

by

Elliott Jost

In Partial Fulfillment
of the Requirements for the Degree
Master of Science in the
George W. Woodruff School of Mechanical Engineering

Georgia Institute of Technology
May 2020

EFFECTS OF SPATIAL ENERGY DISTRIBUTION-INDUCED POROSITY ON MECHANICAL PROPERTIES OF LASER POWDER BED FUSION 316L STAINLESS STEEL

Approved by:

Dr. Christopher Saldana, Advisor
School of Mechanical Engineering
Georgia Institute of Technology

Dr. Kate Fu
School of Mechanical Engineering
Georgia Institute of Technology

Dr. Tom Kurfess
School of Mechanical Engineering
Georgia Institute of Technology

Mr. David Moore
Non-Destructive Evaluation Laboratory
Sandia National Laboratories

Date Approved: November 8, 2019

ACKNOWLEDGEMENTS

I would firstly like to acknowledge my funding sources, including the Department of Energy's support of the Enhanced Preparation for Intelligent Cybermanufacturing Systems (EPICS) as well as Sandia National Laboratories, which both provide crucial financial support for both my graduate education and the success of our research endeavors. Specifically, I would like to thank Mr. David Moore of SNL for his continued support of my research both at Georgia Tech and previously Baylor University in addition to valuable research and career guidance and assistance. I would also like to thank my lab- and office-mates, both for useful and stimulating research conversations and for making Georgia Tech such a fun place to work. Your support and encouragement is not to be understated.

Perhaps most importantly, I would like to thank my parents, whose love, support, and modeling of the Christian life have led me to a place in which I can thrive and pursue my ambitious dreams. Lastly, I would like to thank my wife, Baylee, for her love and encouragement each and every day, without which I might not be in a position to pursue such lofty goals.

TABLE OF CONTENTS

LIST OF TABLES

LIST OF FIGURES

LIST OF SYMBOLS AND ABBREVIATIONS

AM	Additive Manufacturing
CMM	Coordinate Measurement Machine
COD	Coefficient of Determination
CT	Computed Tomography
DR	Digital Radiography
GED	Global Energy Density
LOF	Lack of Fusion
NIST	National Institute of Standards and Technology
PCA	Principle Component Axis
POD	Probability of Detection
ROI	Region of Interest
SLM	Selective Laser Melting
SLS	Selective Laser Sintering
SR	Synchrotron Radiation

SUMMARY

Laser powder bed fusion (LPBF) additive manufacturing (AM) offers a variety of advantages over traditional manufacturing, but the usefulness of AM for manufacturing of high-performance components is currently hampered by internal defects (porosity) created during the LPBF process that have an unknown impact on global mechanical performance. By inducing porosity distributions through variations in print energy density and inspecting the resulting tensile samples using computed tomography and scanning electron microscopy, nearly 50,000 pores across 75 samples were identified. Porosity characteristics were quantitatively extracted from inspection data and compared with mechanical properties to understand the strength of relationships between porosity and global tensile performance. Useful porosity characteristics were identified for reliable prediction of part performance. These results establish an understanding of the complex defect-performance relationship in AM 316L stainless steel and can be leveraged to develop certification standards and improve confidence in part quality and reliability for the broader set of engineering alloys.

INTRODUCTION

Additive manufacturing (AM), the layer-by-layer creation of a part directly from a digital computer-aided design (CAD) model, is a relatively new manufacturing paradigm that is currently coming into maturity for industrial production. Although AM has existed in various forms since approximately the 1980s, recent advances have begun to propel the technology into various production and large-scale manufacturing arenas [1]. The ability of additive manufacturing processes to create parts with complex geometries that are either difficult or impossible to create using traditional, subtractive manufacturing processes such as milling or turning, means that AM is a promising technology for the creation of structures previously not possible. Specifically, metal laser powder bed fusion (LPBF) processes, the focus of this study, have seen significant advancements in recent years.

Additive manufacturing of metals has many potential applications including the light-weighting of components, creation of structures such as functionally graded lattice metamaterials ideal for topology optimization schemes, as well as non-technical benefits such as core capabilities for distributed manufacturing paradigms. Thus far, due to difficulties associated with the safe implementation of AM parts, use has been primarily confined to applications that require highly complex engineering such as those common in aerospace and defense.

Despite the obvious and numerous advantages of additive manufacturing, several key challenges have been preventing the widespread adoption and use of AM technologies. These challenges include surface roughness and surface heterogeneities [2], long manufacturing/print times, limited process scalability, expense of machines and materials,

limited material types, internal defects, and statistical qualification. Technical problems such as surface and internal defects currently plague additive manufacturing processes, making safe implementation of AM parts difficult, while practical issues such as long print times prevent use for production of low-cost components.

Qualification, or the determination of the integrity and quality of a part, is the focus of the present thesis. Qualification inspections cannot be adequately performed to certify a part for use until the effects of common AM problems such as surface and internal defects are well understood. Specific thresholds or models will need to be defined for part certification and cannot be performed without a thorough understanding of the mechanics involved. Surface defects can be largely mitigated via intelligent part design and subtractive machining of part boundaries after printing a component to near net shape. However, many parts either: 1) cannot be designed in such a way that access to machine all part boundaries is possible such as in the case of lattice structures, or 2) necessitate features for post-build machining which limit advantages offered by AM due to time, complexity of path planning, expense, or a variety of other reasons. Internal defects can largely be controlled through post processing by hot isostatic pressing (HIP) and parameter optimization, but their effects cannot be fully removed [3]. Because manufacturing defects cannot be entirely removed from the build process, knowledge of the complex relationship between defects and performance is critical for the safe implementation of AM-produced parts.

Further complicating the process of qualification are the many loading modes in which AM parts may be used, such as in tension, compression, fatigue, bending, shear, torsion, and in more complex loading scenarios in which some combination of these

loading modes may be present. Under different loading conditions, parts experience significantly different stress conditions and failure phenomena depending on material system and load type. Understanding how components will respond in these different conditions will be key for qualifying parts subject to complex loading conditions.

To investigate the relationship between volumetric defects, innate to the laser powder bed fusion AM process, and tensile performance of 316L stainless steel components, tensile sample arrays were built in three different global energy density conditions. Samples were inspected using computed tomography, a nondestructive inspection technique that uses x-ray energy to inspect the inside of components. Following this inspection, samples were tensile tested to gather effective material properties. Next, scanning electron microscopy inspections were performed on the fracture surfaces resulting from tensile testing. Finally, quantitative analysis of porosity using the results gathered from CT and SEM inspections were compared to material properties and correlations were made between porosity defects and tensile performance.

Currently, there exists a gap in model-based understanding of the effects of internal defects on global tensile performance of AM 316L SS and, consequently, an inability to safely and reliable implement or qualify parts. The present research seeks to bridge this gap through correlation of internal defect characteristics and tensile performance metrics. The developed understanding has the potential for enabling a data-driven design of effective inspection processes to help fully realize the potential of additive manufacturing, as will be discussed.

This document is organized as follows: first a background of additive manufacturing qualification, motivation, and previous work will be presented in Chapter 2. Then, an overview of the study and its methods will be discussed in Chapter 3. Chapter 4 presents results from mechanical testing, SEM inspection, and CT inspection as well as a discussion of the significance of these results. Lastly, conclusions will be made, contributions outlined, study limitations addressed, and future works suggested in Chapter 5.

LITERATURE REVIEW

1.1 Introduction to Additive Manufacturing

Although additive manufacturing is currently entering a phase of maturation, the idea of layer-by-layer manufacturing to create complex geometries has existed for over a century, dating back to at least 1902, when George Peacock filed a patent for making composition horse shoes with a layer-by-layer method [4]. However, the birth of modern AM is most often dated by the sale of the first-ever commercialized 3D printing system; the SLA-1 by 3D systems in 1987 [1]. Many AM processes currently exist, including material extrusion, vat polymerization, material jetting, sheet lamination, powder bed fusion, binder jetting, and directed energy deposition [1]. These processes vary widely in mechanics, but all have the common idea of using simple, 2D geometries to create complex 3D geometries. Additionally, this suite of technologies offers a variety of capabilities, from the ability to print parts from the sub-micron scale to hundreds of pounds [1]. Of these methods, metal laser powder bed fusion (LPBF) will be the focus of this thesis, as it offers significant promise for the creation of high-value parts for use in applications demanding highly-engineered components.

While most people associate additive manufacturing, or 3D printing, as it is often called, with small, cheap widgets made of plastic using a desktop system, the metal AM world could not be more different, with commercial machines requiring experienced operators, starting at approximately $250,000, and requiring concomitant safety and post-processing equipment. While polymer-AM has been successfully used for a variety of commercial solutions as well as hobbyist needs, metal AM has a very small number of

successful use cases for high-value, advanced engineering applications, with the 2012 GE Leap jet engine fuel nozzle being one of the most prominent examples [5]. This gap between the technology's potential and successful use is largely due to unknowns relating to qualification or certification of components produced using metal AM technologies.

Metal AM is a desirable manufacturing technique due to its ability to produce components with nearly infinite design freedom, relatively little planning, and a short design-to-production time compared to conventional, subtractive manufacturing techniques which are often limited by tool access and minimum feature size. For example, most AM processes, including LPBF, only require an input stereolithography (STL) file and modification of a few print parameters that remain largely the same across builds, whereas conventional 5-axis machining requires a highly-experienced machinist to create complex path plans using expensive computer aided machining (CAM) software to execute these commands safely and precisely.

Despite its advantages, additive manufacturing is not without drawbacks, producing parts with relatively wide tolerances, poor surface finishes, and at low speed compared to conventional manufacturing processes [6]. Table 1 presents a comparison of various aspects of AM and conventional machining which highlights many of the needs of metal AM. Due to the differences in strengths and weaknesses of AM and conventional manufacturing, hybrid manufacturing systems, which have both additive and subtractive capabilities, are becoming increasingly popular due to their abilities to have the best of both worlds [6–10].

Table 1. Comparison of Additive Manufacturing and Conventional Machining

Aspect	**Additive Manufacturing**	**Conventional/Subtractive Manufacturing**
Surface Roughness	Poor	Excellent
Tolerances	Poor	Excellent
Part Production Time	Long	Short
Design Complexity Capability	Nearly infinite	Limited by comparison
Scrap Rate	Little to none	Large
Necessary Operator Skill Level	Little by comparison	Expert
Production Planning Time	Short	Lengthy if complex

A classic example of additive manufacturing for the creation of a component not possible using conventional machining or manufacturing is architected lattice metamaterials, such as that shown in Figure 1. Lattice structures use designed porosity in building block "unit cells" to architect high strength-to-weight ratio structures. These structures are highly valued in the aerospace industry where low weight is a crucial aspect of successful design. Furthermore, lattice structures offer the ability for topology optimization, in which a parameter such as unit cell density, strut size, or unit cell size is modified to optimize the desired use of that component, whether it be structural loading capability or heat transfer [11].

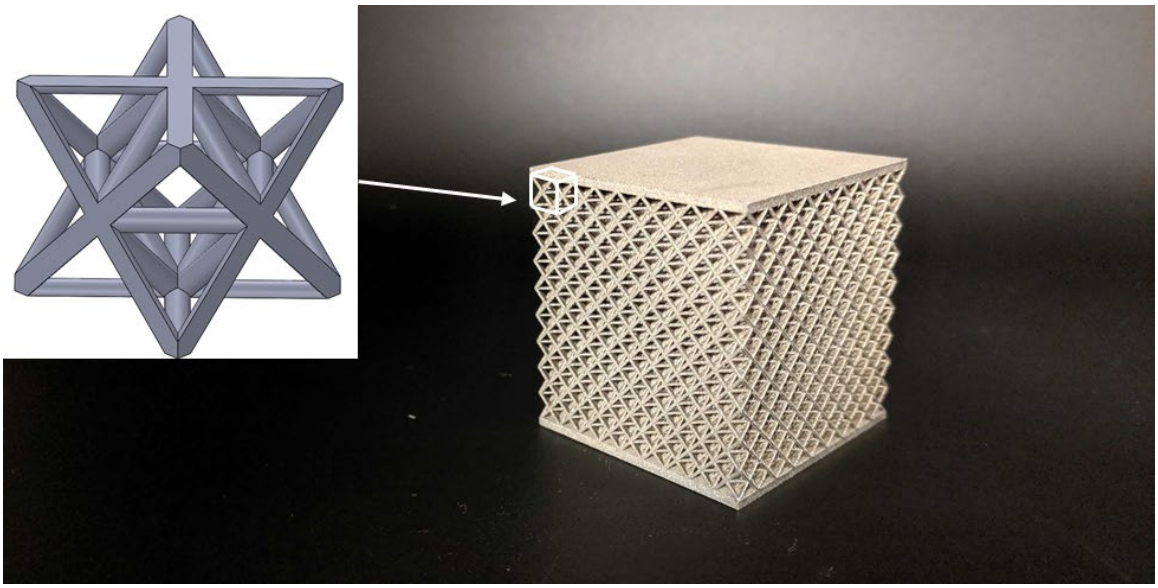

Figure 1. AM 304L SS lattice metamaterial structure not possible to create using conventional manufacturing. Repeating unit cell geometry shown as CAD model.

The design freedom offered by additive manufacturing makes components such as lattice structures possible. However, despite all the advantages offered by AM, qualification of complex parts such as lattices is an equally challenging task. Geometric and internal feature qualification of these parts, which have dozens to tens of thousands of individual struts, is a daunting task. Lattices present an extreme example of the difficulty of qualification for AM components because of their complexity. These topics and their needs will be presented in more detail later in this chapter.

1.1.1 Laser Powder Bed Fusion

Laser powder bed fusion (LPBF), the AM technique used to manufacture the samples presented in this thesis, involves the selective, localized joining of a layer of powdered metal using a high-energy laser. LPBF is often referred to as selective laser sintering (SLS) or selective laser melting (SLM) for this reason. The LPBF technique allows for the

manufacture of features down to a few tens of microns, however, it has been demonstrated that features below 500 μm in size for 316L SS can result in mechanical properties dominated by geometric heterogeneities common at this size scale if print settings are not optimized [2]. The advantages offered by LPBF as well as the widespread commercial availability of machines, have established it as the primary metal AM technique. A more in-depth of the mechanics of the LPBF process will be presented in the Manufacture of Samples section of Chapter 3.

1.2 Qualification and Inspection

Qualification, often called certification, is a crucial aspect of any manufacturing process. Qualification of additively manufactured components can take on many methods, focusing on feedstock powder [12,13], in-situ melt pool monitoring [14,15], geometric [16], internal feature [5,17–20], and material property [21], all of which inspect or monitor crucial aspects of the laser powder bed fusion additive manufacturing process. Currently, additive manufacturing qualification is typically performed through a "certification by test" process, in which extensive and costly testing is performed on components to certify a specific part for the specific loading and operating conditions it will be see during use. This paper aims to shift the AM qualification paradigm from "certification by test" to "certification by analysis," in which material models and extensive knowledge of material performance are leveraged to qualify AM components through deterministic methods, by gaining an improved understanding of defect-property relationships in 316L SS produced by AM. This paradigm shift would allow for shorter part development times as well as safer implementations of AM components. As an introduction to current AM qualification

methods and the steps necessary to shift to the “certification by analysis” paradigm, two types of qualification will be discussed: geometric and internal feature.

1.2.1 Geometric Qualification and Inspection

Geometric qualification involves inspection of a part through the precise measurement of features of a part or assembly that ensure: 1) a part will fit and interact with other components properly in its assembly and 2) geometry of the part is within tolerances that allow it to perform according to design. Geometric qualification is done through dimensional metrology methods, and typically includes tactile measurements with a coordinate measurement machine (CMM), which takes measurements accurate to the sub-micron level by contacting a part with a probe, or through non-contact measurements using a structured light scanner, which projects fringe light patterns on a part and interprets surface contours based on the distortion of the fringe pattern. A recent review by Leach et al. [16] highlights some of the many challenges facing geometrical metrology for metal additive manufacturing. In this review, the authors discuss internal feature metrology, which will be presented in the following section, as well as place heavy emphasis on the need for standardization of metrology for metal AM. Several other papers highlight the need for qualification standards in AM [5,17,22–24]. The establishment of standards is crucial for the advancement of AM technologies and the widespread adoption of these methods in industry at large. Perhaps most importantly, qualification performed using a standard provides confidence for both the manufacturer and the customer in the integrity of that part, something sorely lacking in the current AM world. This thesis intends to gain understanding of the defect-property relationship to aid in the establishment of inspection standards not for external feature geometrical metrology, but for internal defect inspection.

1.2.2 Internal Defect Qualification and Inspection

The focus of this thesis is the inspection and subsequent qualification of a part based on internal features and allowable internal defects. Many studies have been performed to consistently and reliably use CT inspections for quantitative measurement of either geometric or internal features. In a review by Maire and Withers [25], CT softwares used for pore identification are discussed. These softwares include ImageJ, Avizo, Morpho+, Pore3D, Blob3D, Imorph, and VGSTUDIOMAX, the last of which is used in this thesis. Additionally, researchers at the National Institute of Standards and Technology (NIST) proposed a standardized method for porosity quantification and metrology relying on Bernsen's method, an local threshold algorithm [26]. This method was tested on additively manufactured cobalt chromium material and performed well when compared to standard thresholding algorithms such Otsu's and Yen's method. Standardization of methods for internal feature metrology is crucial for consistent part assessment across CT inspection systems.

Challenges for quantitative computed tomography, ideal for AM measurement of internal and external features of a part, include the lack of standardized, deterministic methods for surface determination and internal feature recognition. Surface determination involves the segmentation of two materials, most often the material of the object of interest and air, to accurately determine the surface of an object. Surface determination is most often done through simple iso-value thresholding, in which pixels with grayscale values below the threshold are designated as air and those above as material, or vice versa. Scan contrast, beam hardening, and user interaction can all effect the determined surface. More complex surface determination methods exist that are available in CT analysis softwares

such as Volume Graphics, however they are often black boxes or opaque to the user. Similarly, internal feature (e.g. porosity) identification, can be done with simple thresholding or with more complex algorithms. These more advanced algorithms often take into account local contrast variations in addition to global contrast as well as shape and size constraints to distinguish between true pores and image artifacts such as beam hardening, ring artifacts, or streaking. Like surface determination algorithms, many are available in commercial software, and are black boxes. To be sure, many advanced CT users, particularly within academia, create their own algorithms for internal feature recognition and surface determination, however these algorithms are very much limited to the most advanced users and require extensive expertise to use properly.

1.3 Pore Type, Formation, and Mitigation

Porosity is a major issue in LPBF AM and is, in general, poorly understood. Despite bulk porosity values often being very low with part densities >99%, pores can still have significant impact on part performance [13]. Three main types of porosity: gas porosity, lack of fusion, and keyhole, have been identified to be common in this process, all of which will be detailed here. Gas porosity, by number of pores, is the most common type of porosity found in AM components due to its existence in the raw powder. These small, spherical pores can form by two mechanisms: via entrapped gas from the gas atomization process, or by the entrapment of inert build chamber or shielding gas inside the fused material [27]. Regardless of the mechanism of formation, gas porosity tends to be very small but much more numerous compared to lack of fusion or keyhole porosity. Gas porosity, due to its small size and spherical shape, is often assumed to have a relatively

small effect on part performance compared to LOF pores, however this has not been thoroughly proven, and effects of clustered or concentrated gas porosity is still unknown.

Lack of fusion porosity, in contrast to gas porosity, tends to be very random in shape due to its formation mechanism. Lack of fusion defects are often categorized separately from porosity in the literature due to their unique mechanism of formation. However, for the purposes of uniformity, this thesis will refer to these as pores. These pores are characterized by sharp edges and webbed, elongated paths. Due to their sharp edges, LOF pores often act as stress concentrators and are suspected to be particularly detrimental to mechanical performance under fatigue loading conditions [27]. Lack of fusion pores are formed by, as the name suggests, a lack of fusion of two melt paths. If a melt path is too far from its neighboring melt path, either on the same layer or the layer below, the two may not fuse together. Similarly, melt paths that are too small and are not wide enough to join their neighboring melt paths or have insufficient laser power or energy density and thus cannot fully fuse to the previous layer, can result in LOF porosity. This failure to fuse melt paths or layers entirely can result in LOF pores with an unpredictable shape.

Lastly, keyhole porosity is formed during the LPBF process when energy density is too high [28]. This excess of energy per unit area or per unit volume results in evaporation of the metal and formation of plasma, which causes a vapor cavity that results in entrapment of gas and therefore voids [29,30]. Specifically, keyhole formation occurs when the melt pool transitions from conduction mode to keyhole mode laser melting in LPBF, which occurs when a normalized enthalpy threshold is exceeded [30]. In this same paper, normalized enthalpy was shown to be a function of several print parameters, including power, speed, and beam size, key parts of global energy density. Depending on

the energy density, pores can be spherical in shape or shaped as a “keyhole,” as the name suggests in the most extreme cases. Keyhole porosity is a relatively well-understood phenomenon, having been an issue in traditional welding and laser cladding prior to the advent of metal AM.

With a general understanding of the formation methods for gas, LOF, and keyhole porosity, one can begin to prevent their formation. Gas porosity is largely determined by gas pores existing as a result from the metal atomization process. Thus, steps must be taken during the process of creating metal powder to mitigate gas porosity. This can largely be done through the use of high-quality powders. To mitigate LOF porosity formation, mapping of print parameters can yield optimal processing conditions that will ensure paths and layers are fully fused. Lastly, keyhole porosity can be prevented through careful tuning and control of laser parameters to ensure melt pools stay in conduction mode melting. Additionally, printer manufacturers are currently implementing laser power and speed modulation to control energy density and mitigate keyhole porosity formation. Monitoring and control is often attempted through cameras coaxial with the laser [14,15,31–40], however reliable closed-loop feedback control of laser parameters is not currently possible. Development of charts such as that in Figure 2 can be used to facilitate the manufacture of optimal parts with minimal internal defects.

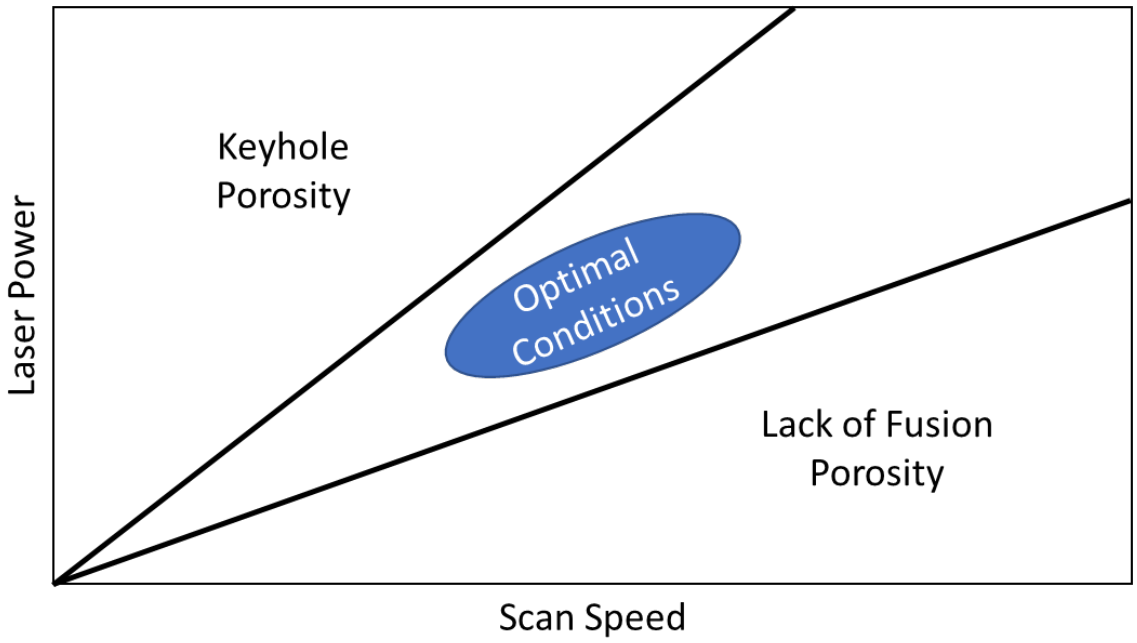

Figure 2. Processing Map showing optimal processing conditions to eliminate porosity.

1.4 Correlation of Mechanical Properties

Despite in-depth knowledge about the formation of porosity, very little is currently understood about the relationship between internal defects, colloquially referred to as porosity, and part performance in various loading conditions. Many studies have been performed in this area, but many rely on non-rigorous, non-quantitative inspection of components, instead opting for generalized measurements such as total pore count and bulk density. Large focus has been placed on fatigue performance of AM structures, primarily using Ti6Al4V [41–47], AlSi10Mg [48–51], and Inconel 718 [52,53], common materials used in the aerospace industry. However, some fatigue studies have used 316L SS [54], the material of interest in the present study.

Additionally, studies have been performed relating defects and tensile performance, as in this thesis [19,20,55–59]. These studies have covered a variety of materials including

316L SS, Ti6Al4V, AlSi10Mg, Inconel 718, and 17-4PH SS. For example, Madison et al. [55] examined dozens of 17-4PH tensile samples inspected using computed tomography and compared these results to tensile performance. This study examined porosity distribution characteristics including total number of defects, equivalent spherical diameter, volume, among others and found that relatively low correlation values were found, the maximum being a coefficient of determination (COD) of 0.50. Slightly better success was had when multiple pore parameters were combined, reaching a maximum COD of 0.60. Boyce et al. [19] utilized extreme value statistics to reveal failure-critical defects in 17-4PH SS subject to tensile loading. Examining over 1000 samples, this study emphasized the need of large sample set sizes for characterization of the stochastic behavior of AM materials.

Others have utilized in-situ CT testing, in which a test is performed inside of a CT machine to monitor a process in pseudo-real-time and track defect evolution, as in Ref. [56], which performed tensile testing in a synchrotron radiation (SR) source. This study utilized SRCT to track three-dimensional pore volume, distribution, and morphology throughout tensile testing. Using this high-resolution method, defect elongation was observed within samples. Conclusions of this study involved emphasizing the insufficiency of bulk density and porosity measurements made using the Archimedes method and the importance of accounting for pore distributions. However, this study did not elucidate the complexities of the defect-property relationship in samples without designed pore distributions. A study by Miers et al. [58] examined 316L SS tensile samples with “natural” porosity resulting from the build process and developed an algorithmic approach to predict tensile failure location using a fracture mechanics-based factor approach. This study

offered promising results towards understanding the role of pores as stress concentrations in AM.

In a study by Dressler et al. [2], computed tomography and scanning electron microscopy were utilized to observe and identify trends involving an increase in the number and intensity of geometric heterogeneities as feature size decreases. These defects, which often extended to both the interior and exterior of the samples, were observed to have more significant effects on performance in tension at small size scales than at larger size scales. Thus, scalability will be a significant challenge as AM advances forward, particularly due to the small components often manufactured using AM.

In another study, Kramer et al. [20] examined the effects of porosity in 316L SS on fracture properties. Interrupted tensile testing and CT inspection were used to observe the evolution of voids and cracks at various stages of tension. In this study, the authors focused largely on the total number of voids seen through both CT and SEM and concluded that "despite a lack of correlation between aggregate AM voids and global mechanical behavior, the AM voids influenced local crack initiation and growth".

In summary, many studies have been performed in efforts to understand the influence of porosity on global mechanical behavior. Due to a combination of confounding variables such as surface roughness and build orientation, lack of thorough inspections and systematic studies correlating defects and performance, the influence of internal porosity on global behavior largely remains a mystery. Through thorough inspection and systematic study, the author aims to elucidate the defect-property relationship to shift the AM inspection paradigm to certification by analysis.

METHODS

1.5 Introduction

To elucidate the relationship between internal defects and tensile performance, a variety of inspection and testing methods were required. In this section, these methods will be presented in the order in which they were performed; the manufacture of samples, computed tomography inspection and analysis, high-throughput mechanical testing, scanning electron microscopy inspection, and quantitative fractography analysis.

1.6 Manufacture of Samples

Samples used in this study were built in three different spatial energy density or GED conditions using an EOS M 290 additive manufacturing machine equipped with a 400 W IPG Photonics Laser. The type of AM process this machine uses is called laser powder bed fusion, which entails a cycle involving the application of a thin layer of powdered metal, typically on the order of 10-50 μm, via a metal recoater blade, followed by a laser melting the powder in the shape of the slice for the desired part at that height. Following the melting of the powder, the build plate is incremented downward in the z-direction and the cycle repeats. Figure 3 presents a diagram showing a brief overview of the LPBF AM process used to manufacture the samples used in this study.

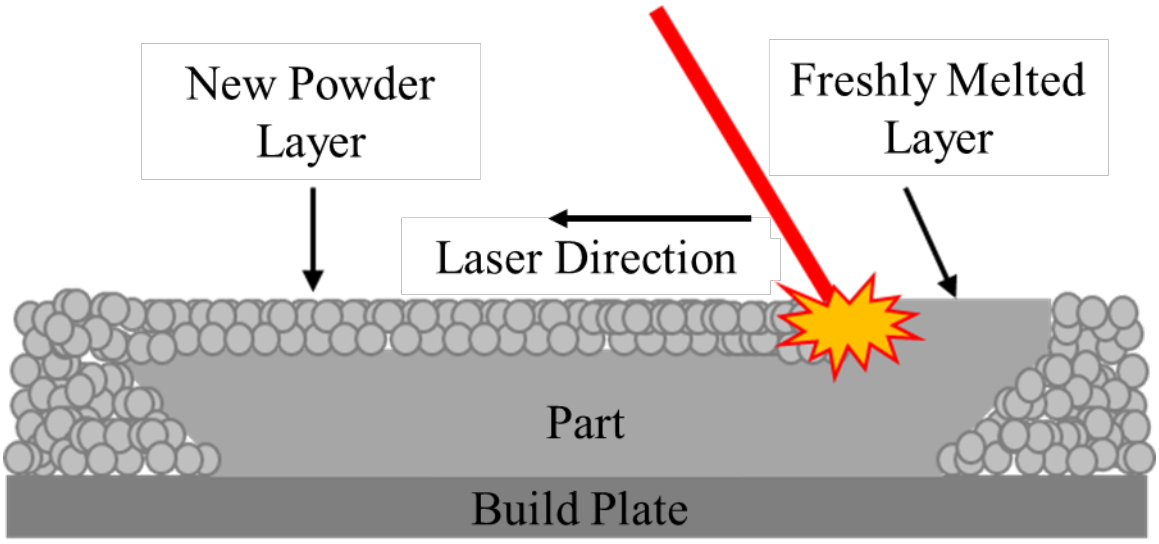

Figure 3. Laser Powder Bed Fusion Diagram

Three different global energy density (GED) conditions were examined in this study. GED, a measure of the energy input per unit area, can be defined using Equation 1,

$$GED = \frac{PH}{S} \tag{1}$$

where P is laser power, H is hatch spacing, or the distance between parallel melt paths, and S is laser speed. GED is most often reported in $\frac{J}{mm^2}$ and is commonly approximately 2.0 $\frac{J}{mm^2}$ for 316L SS. Global energy density is the two-dimensional equivalent of volumetric energy density, which includes laser thickness as a parameter in the denominator and is commonly used to understand AM builds. Layer thickness was kept constant in this study, so it can be assumed that GED and volumetric energy density would provide identical trends and only be different by a scaling factor of $\frac{1}{t}$ where t is layer thickness.

In this study, hatch spacing and laser speed were kept constant throughout builds and across build plates. Laser power was changed by +/- 25 W across build plates from the nominal 195 W to alter GED, the independent variable investigated in this study. 316L stainless steel was used as the material with nominal particle size in the range of 30-60 µm. No post processing heat treatment or HIP was performed and samples were evaluated in the as-built state. Table 2 presents the GED parameters used to print the samples used in this study.

Table 2. GED Parameters Used to Print Samples

	P (W)	**H (mm)**	**S (mm/s)**	**GED *(J/mm^2)***
High GED	220	0.09	1083	***2.26***
Nominal GED	195	0.09	1083	***2.00***
Low GED	170	0.09	1083	***1.74***

Figure 4a presents a CT scan of an array of 25 tensile samples. The reason for this specific sample geometry and size will be discussed in the High-Throughput Mechanical Testing section of this document. Figure 4b shows an image of the build plate with the sample array of interest highlighted in red.

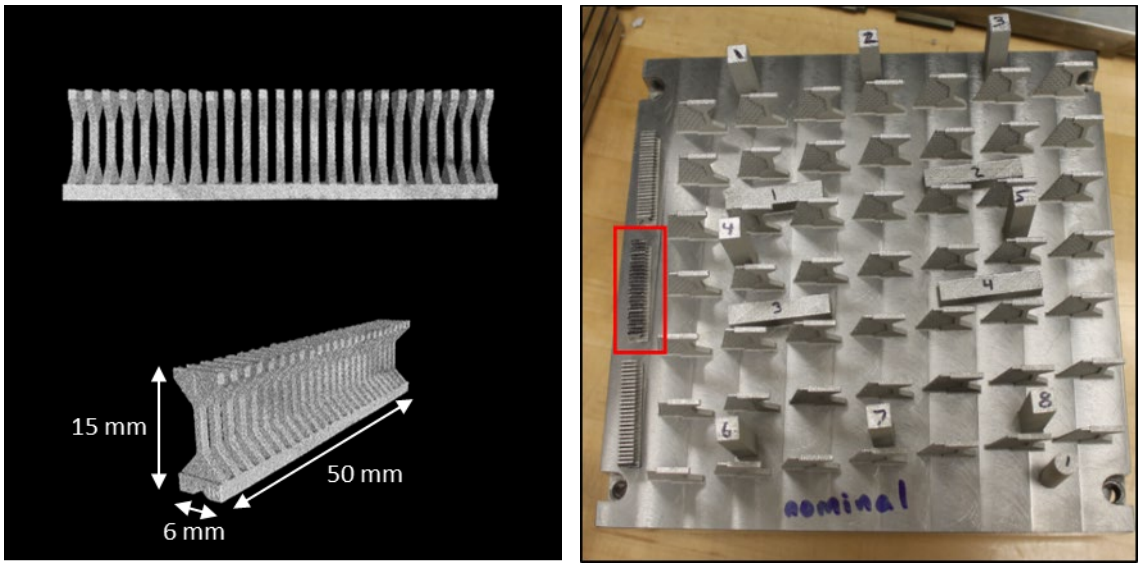

a) b)

Figure 4. Images of Built Samples. a) CT scan of sample array with dimensions, b) Nominal GED Build Plate

1.7 Computed Tomography

Computed tomography (CT) is a common technique for nondestructive inspection of a variety of parts from metals to polymer composites, but is most well-known for its use in medicine. CT is a well-suited method for inspection of AM components due to its ability to nondestructively investigate the internal structure of components with high resolution. Laboratory CT machines such as those used in this study, can commonly achieve resolutions of 5-15 µm at their highest resolution, depending on part size and material.

Computed tomography consists of a series of x-ray radiographs (projections) being taken of an object through a 360º path. Using reconstruction algorithms such as the standard filtered backprojection method, these radiographs can be assembled into a three-dimensional object in which the gray scale value of each pixel is roughly proportional to

the density of the material represented by that pixel. Attenuation of the x-ray is exponential and is described by Equation 2,

$$I = I_0 e^{-\mu x} \tag{2}$$

where I is the final x-ray energy directly proportional to the grayscale value of the radiograph, I_0 is the initial energy, x is the distance traveled through a component, and μ is an attenuation coefficient that includes factors such as density and microstructure.

1.7.1 Computed Tomography Inspections

In this study, a Nikon M2 Dual Head 225/450 kV computed tomography machine equipped with a Perkin Elmer detector was used to inspect the three sample arrays. Due to the elongated geometry of the arrays, a helical scan path was chosen in which the sample simultaneously rotates and raises along a helical path. The helical scan pattern allowed for higher resolution data to be obtained for the object in a single scan as opposed to the conventional circular scan path. Figure 5 presents x-ray projections used to reconstruct the 3D CT volume, which show the helical scan path used.

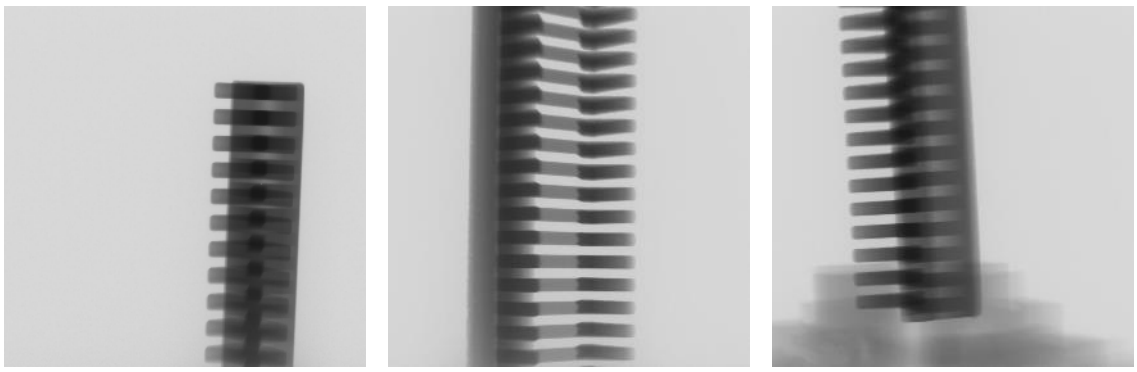

Figure 5. Raw X-Ray Projections Showing Helical Scan Path

Figure 6 shows the setup used for computed tomography inspection. Sample array fixturing is shown in Figure 6a, the outside of the Nikon system used for inspection is shown in Figure 6b, and the 450 kV x-ray source with copper prefiltering is shown in Figure 6c.

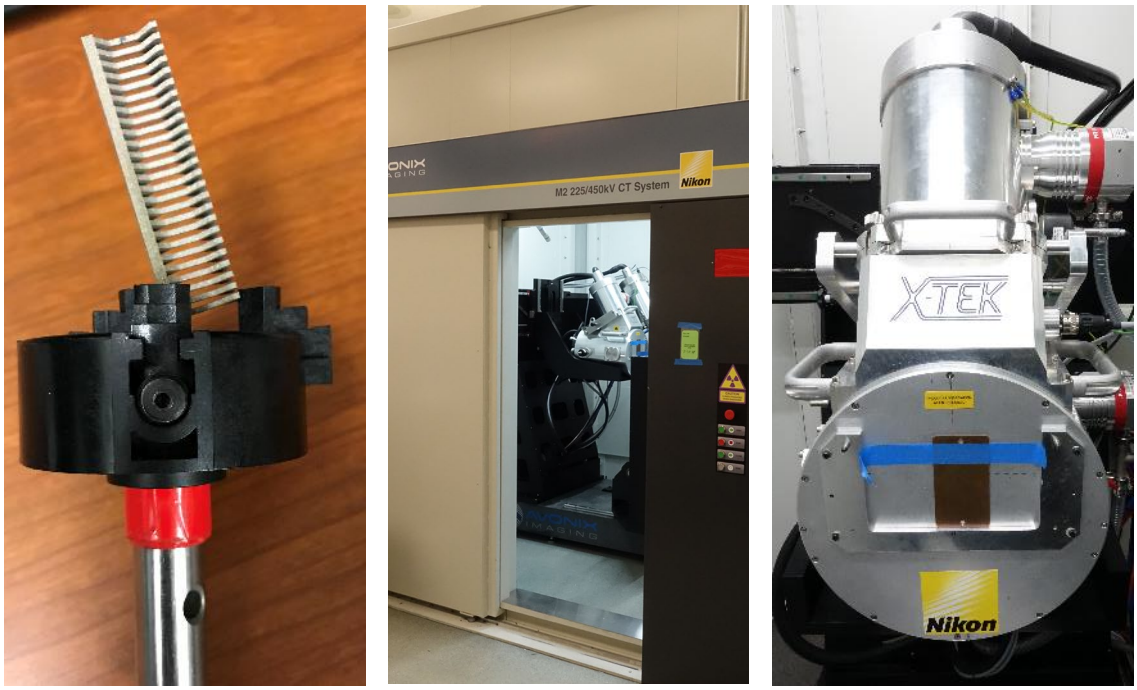

a b c

Figure 6. Computed Tomography Inspection Setup. a) Sample array fixturing. Silver cylinder is held vertically in CT system for fixturing. b) Nikon CT system. c) 450 kV x-ray source with Cu prefilter attached.

For these scans, the 450 kV x-ray source was used operating at 440 kV. Eight frames were averaged to obtain each of the 2294 x-ray radiographs used for reconstruction. A voxel side length of 10 µm/voxel was achieved, which allowed for resolution of shape of identified pores. A 1 mm Cu prefilter was used to mitigate beam hardening effects caused by the naturally polychromatic energy spectrum of laboratory x-ray sources. Table 3 summarizes CT parameters used for these inspections. Reconstruction of these inspections was performed using Nikon Metrology X-Tek CT Pro 3D.

Table 3. CT Inspection Parameters

Parameter	**Value**
Number of Projections	2294
Voltage	440 kV
Current	227 µA
Prefiltering	1 mm Cu
Resolution	10 µm/voxel

1.7.2 Analysis and Registration

Analysis of CT data was performed in Volume Graphics VGSTUDIO MAX 3.2, a CT data analysis suite. The scanned arrays were initially segmented using a standard ISO-50 threshold technique, which uses the average gray value between histogram material and air peaks. In an effort to determine surface contours of the material most accurately, this initial segmentation was followed by an advanced surface refinement technique built into the software that uses a deformable surface technique. Noise particles and voids were removed during the surface determination process.

To digitally register the CT volumes, theoretical surfaces were fit to geometric features on the volumes. By defining these features, registration can be performed reliably and consistently. For these samples, planes were defined and intersected to form lines and points such that the sample gage sections were aligned with the z axis, the bottom plate was defined by the x-direction in the axial direction and the y-direction in the transverse direction. Planes were defined by using fit points shown in Figure 7a to match the coordinate system defined in this same figure.

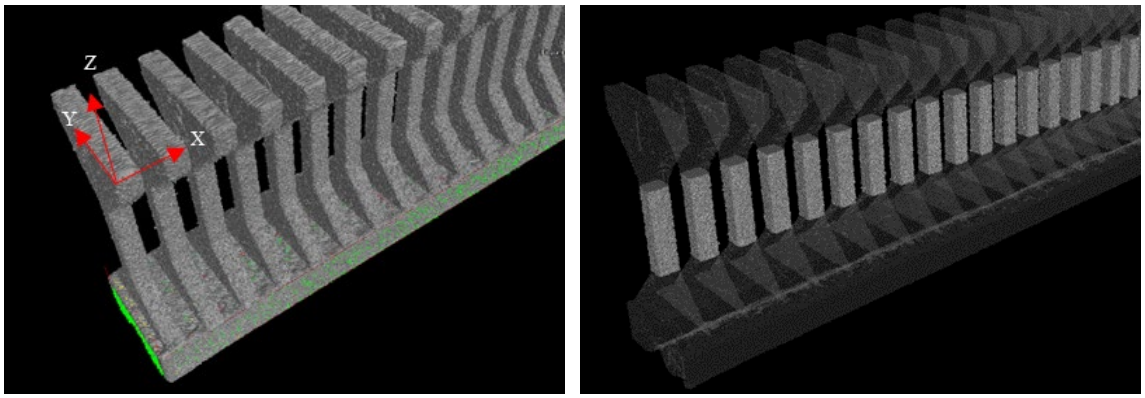

a) b)

Figure 7. Digital Registration of CT Volumes. a) Coordinate system and fit points shown in green used to define geometric features. b) Semi-transparent samples to highlight gage sections used for analysis.

For consistent individual porosity assessment, the 25 gage sections on each tensile sample array were mathematically defined using the coordinate system shown in Figure 7a. A rectangular prism region of interest (ROI) was created to separate the gage section of each sample. Boolean intersection of this ROI and the segmented material allowed for the attainment of a single unified ROI that encompassed the exact contours of each gage section. Figure 7b shows the array volume with the gage sections 0% transparent and the rest of the array semi-transparent.

To identify porosity in each sample, VGDefX, a Volume Graphics built-in porosity identification algorithm was used. A 2-voxel offset from the determined surface was used in combination with a medium adaptive noise reduction scheme to ensure noise or edge artifacts were not misidentified as pores. Furthermore, ranges for the parameters of probability, pore diameter, compactness, and sphericity ranges were defined to identify true pores and avoid misidentification of image artifacts as pores. These criteria are presented in

Table 4.

Table 4. Parameters used in CT analysis to identify realistic porosity

Probability	Diameter (mm)	Compactness	Sphericity
>0.85	0.0625-1.00	0.08-1.00	0.13-0.65

1.8 High-Throughput Mechanical Testing

Mechanical testing of samples was performed using a custom, high-throughput tensile testing system that allows for the automated, rapid testing of tensile samples. This system encompasses a modified MTS servo-hydraulic load frame equipped with an Interface 2-kip load cell. To automate testing, a mounting stage for sample movement was created that will position a new sample after the previous sample was tested. A tube connected to compressed air is positioned to blow the top of a pulled sample out of the way prior to the stage progressing to the next sample. The sample array geometry, dimensions of which are shown in a drawing in Figure 8, was used in this experiment and designed to make the testing fast and efficient. Wedge grips were used to quickly and easily grab the samples as detailed in the ASTM E8 standard. Sample movement was automated using a KeLing Technologies, Inc. stepper motor and a Temposonics position sensor. Depending on material, 50-100 samples can be tested per hour. Figure 9 provides a diagram of the testing setup used for mechanical property characterization. Further details on this stage can be found design of this testing stage can be found in Ref. [60].

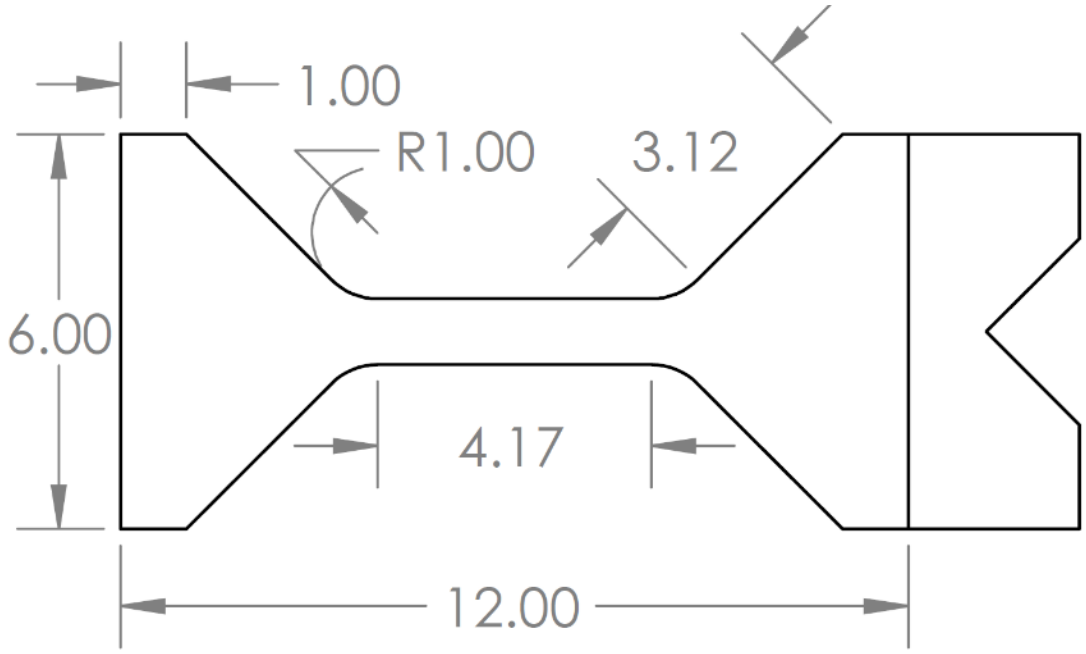

Figure 8. Drawing of Dogbone samples used. Dimensions in mm. Samples are 1mm thick.

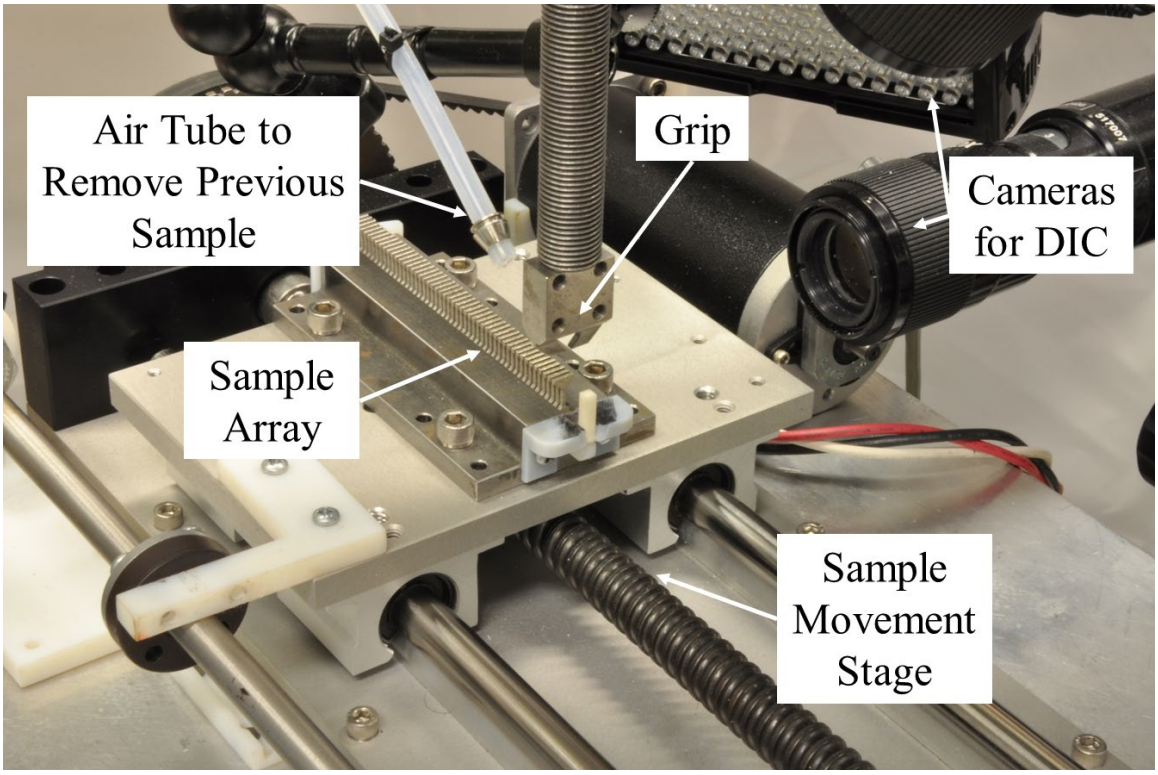

Figure 9. High-Throughput Tensile Testing Setup

Two cameras, one normal to the sample face looking down the +x-axis and one along the +y-axis, were used for real-time digital image correlation (DIC) strain tracking using VIC-Gauge software by Correlated Solutions. This allowed for further automation by using non-contact strain measurements as opposed to traditional contact extensometers. A pixel-to-millimeter ratio was established using a reference image containing an object of known dimensions and applied as a scaling factor to ensure the accuracy of measurements. Cross-sectional area was measured using these cameras. An image of the automated measurements from the y-axis camera is shown in Figure 10.

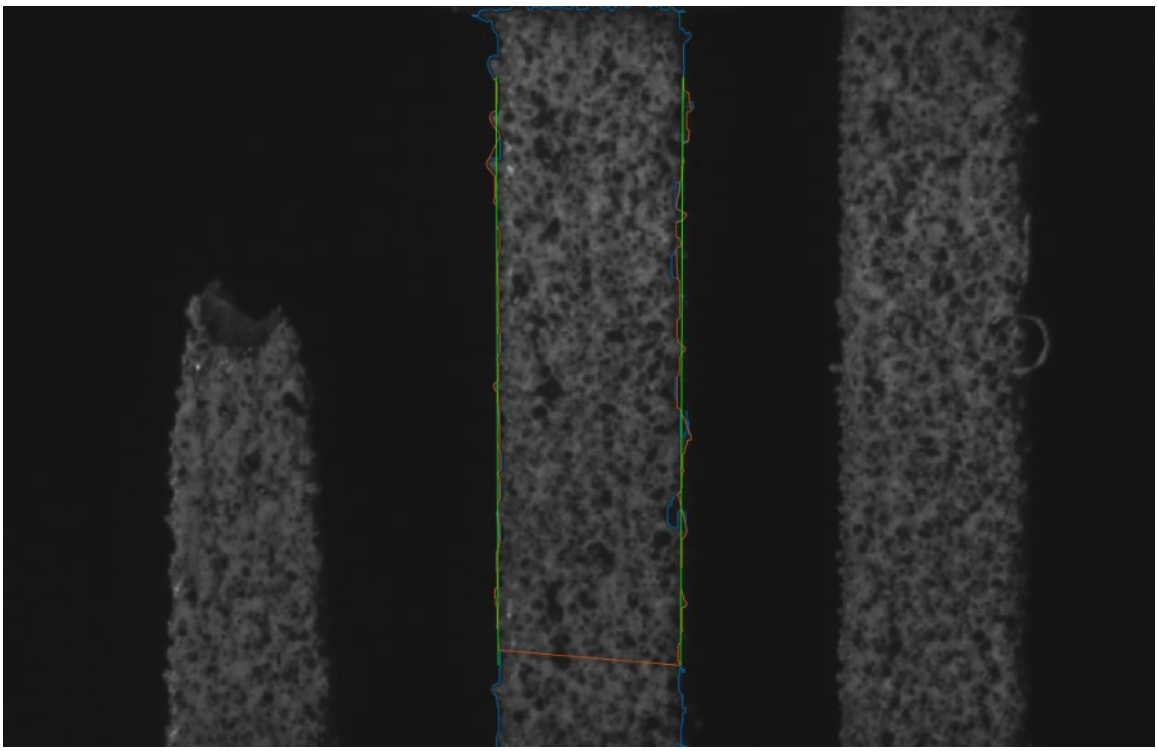

Figure 10. DIC Measurement of Gage Section for Cross-Sectional Area Calculation

To aid in DIC measurements, samples were speckled with a white undercoat and a black speckle pattern via spray paint. Samples were pulled at a constant rate of 0.03 mm/s, a rate which was verified by the DIC solution. From this tensile data, mechanical properties

were extracted. Properties calculated were: ultimate tensile strength (UTS), strain at UTS, ductility, modulus, yield stress, and strain at yield. Ultimate tensile strength was calculated by finding the highest engineering stress value reached and the strain at this point was recorded. Ductility was the percent strain at failure and modulus was determined by finding the slope of the elastic loading curve. Yield strain was calculated as the strain by intersecting a line parallel to the modulus with an x-intercept at 0.2% offset.

1.9 Scanning Electron Microscopy

To investigate the fracture surfaces formed during tensile testing, scanning electron microscopy was employed because of its ability to provide ultra-high resolution images of fracture surfaces on the order of single micron-resolution. The top and bottom fracture surfaces of tested samples were assumed to be complementary, thus providing mirrored and roughly identical information about porosity. Consequently, only the bottom fracture surfaces, those still attached to the array, were imaged. This provided the additional benefit of ensuring that all 150 fracture surfaces would be imaged using the same coordinate system and were thus comparable between images without needing to account for orientation differences. Figure 11 presents representative images of porosity investigation seen in this study and shows the ability of SEM inspection to resolve very small features. Figure 11a shows several small pores clustered together and Figure 11b shows a single pore up close. In this image, surface roughness likely created by melt pool tension can be seen on the interior of the pore.

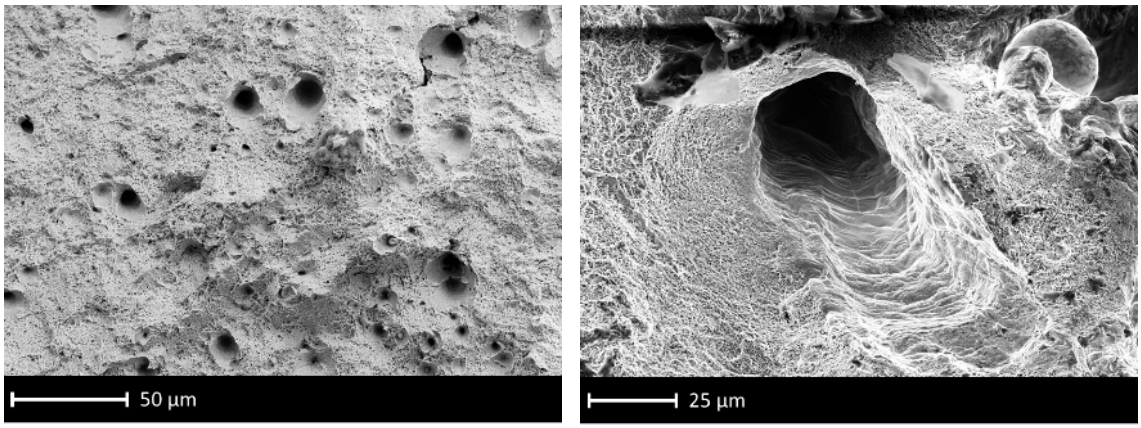

a b

Figure 11. Examples of fracture surface images obtained with SEM. a) Clustered porosity assumed to be gas porosity. b) Close up of pore with melt pool lines visible in inside of pore.

A Zeiss Ultra 60 Field Emission Scanning Electron Microscope (SEM) equipped with a Schottky FEG gun was used for fractographic inspection. Fracture surfaces were imaged with an acceleration voltage of 15 kV using the secondary electron detector to extract as much topographical information about the fracture surfaces as possible using SEM. A relatively large working distance of approximately 8 mm was used, which provided a depth of field that encompassed the majority of the surface and ensured that measurements of pores at all points could be made with comparable accuracy. Figure 12a shows the Zeiss Ultra 60 SEM used for fracture surface inspection. Figure 12b shows the fracture surface arrays placed in a plasma cleaner used to remove organic matter from the surfaces that would obscure features of interest.

a b

Figure 12. SEM Inspection a) Zeiss Ultra 60 SEM Used for fracture surface inspection b) Samples placed in plasma cleaner to remove residual organic matter on surface

1.9.1 Quantitative Fractography

This study aimed to employ quantitative fractography to investigate the different types of porosity in 316L SS, characterize this porosity, and develop an in-depth understanding of how these defects are correlated with tensile performance through quantitative image feature extraction. To do so, FIJI, an ImageJ analysis package, was used to inspect pores seen on the fracture surfaces of the samples of interest. Using FIJI, low-magnification images of approximately 250x and a resolution of ~3 μ/pixel were used for quantitative assessment. Figure 13a shows an example of a fracture surface inspected in this study. With high-resolution imaging, even pores with diameters in the ~10 μm range can be readily identified. Higher magnification images, such as Figure 13b where magnification of 2,240x reveal detailed information about a microscopic pore.

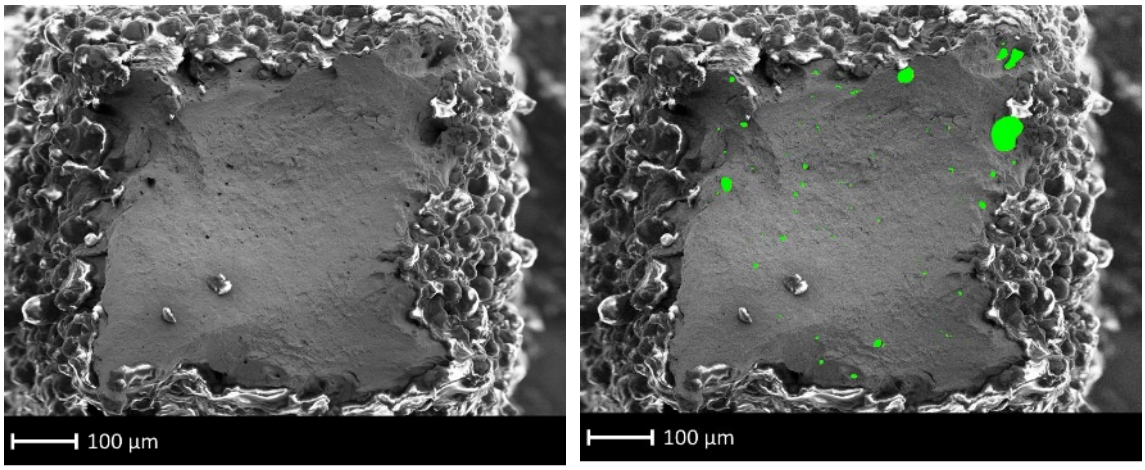

a b

Figure 13. SEM-Identified pores. a) No overlay image. b) Green overlay of identified pores used for feature extraction.

Using FIJI, quantitative pore characteristics were extracted. Extracted characteristics include maximum diameter, area, x- and y-centroid locations, bounding box location and size information, circularity, and roundness. These statistics were exported to MATLAB for later analysis and comparison with CT analysis results and mechanical properties.

RESULTS & DISCUSSION

This chapter is organized such that results will be presented in their entirety and will be followed by a discussion of the underlying nature of the observed phenomena. The results and their implications for the implementation of AM components in high-performance systems will be discussed. Additionally, comparison of results to those of other studies will be presented and any discrepancies in results discussed. In this way, results may be understood insofar as they apply to qualification of AM components and the future of additive manufacturing.

1.10 Mechanical Properties

High-throughput mechanical testing allowed for the understanding of the effects of different energy density conditions on mechanical performance to be evaluated. Properties obtained from tensile testing include the geometric property of cross-sectional area (measured optically with cameras in the high-throughput tensile testing setup), ultimate tensile strength (UTS), ductility, modulus obtained from unloading and reloading during the testing, yield stress, and strain at yield. Table 5 presents mean values for each property by GED type as well as the associated standard deviations.

Table 5. Experimental Summary for All GED Levels (Mean ± Population Standard Deviation)

Mean Value	X-Sectional Area (mm^2)	UTS (MPa)	UTS Strain (%)	Ductility (%)	Modulus (GPa)	Yield Stress (MPa)	Yield Strain (%)
High GED	1.225±0.034	490±13.4	45.2±2.7	60.7±3.59	127.3±3.6	337±19.0	46.9±1.5
Nom GED	1.166±0.032	481±12.9	54.5±2.7	70.9±3.68	124.3±3.2	358±18.4	49.4±1.6
Low GED	1.107±0.028	494±11.3	56.5±2.3	73.6±3.76	133.2±3.3	366±18.0	48.1±1.5

From Table 5 it can be observed that variability in performance tended to be higher for UTS, UTS strain, ductility, modulus, and yield stress as indicated by the standard deviation among the high and low GED samples as compared to the nominal GED samples. This is important because understanding the reliability of a component is critical to its qualification process. Additionally, ductility in the high GED samples was observed to be 15-19% lower than in the nominal and low GED samples at 60.7% vs 70.9% and 73.6%, respectively. This drop in ductility will be put into the context of porosity defects later. Cross-sectional area is also seen to be highest in the high GED samples at 1.225 mm^2 compared to 1.166 mm^2 and 1.107 mm^2 for the nominal and low GED samples. This is suspected to be a result of the large melt pool created by the extra-high energy laser.

1.11 Scanning Electron Microscopy

Scanning electron microscopy inspection of the resulting fracture surface allows for an improved understanding of how the samples fractured. The magnification offered by SEM imaging results in high-quality, high-resolution images of microscopic details occurring on the fracture surfaces such as porosity, ductile dimples, and cracking. A visual summary of pores identified during visual inspection of the SEM-imaged fracture surfaces is shown

below in Figure 14. In this figure it can be seen that the samples produced in the high GED condition tend to have very large pores compared to the nominal and low GED samples. Additionally, these large pores tend to cluster toward the edge of the sample fracture surfaces. Both trends will be demonstrated shown later in SEM and CT results.

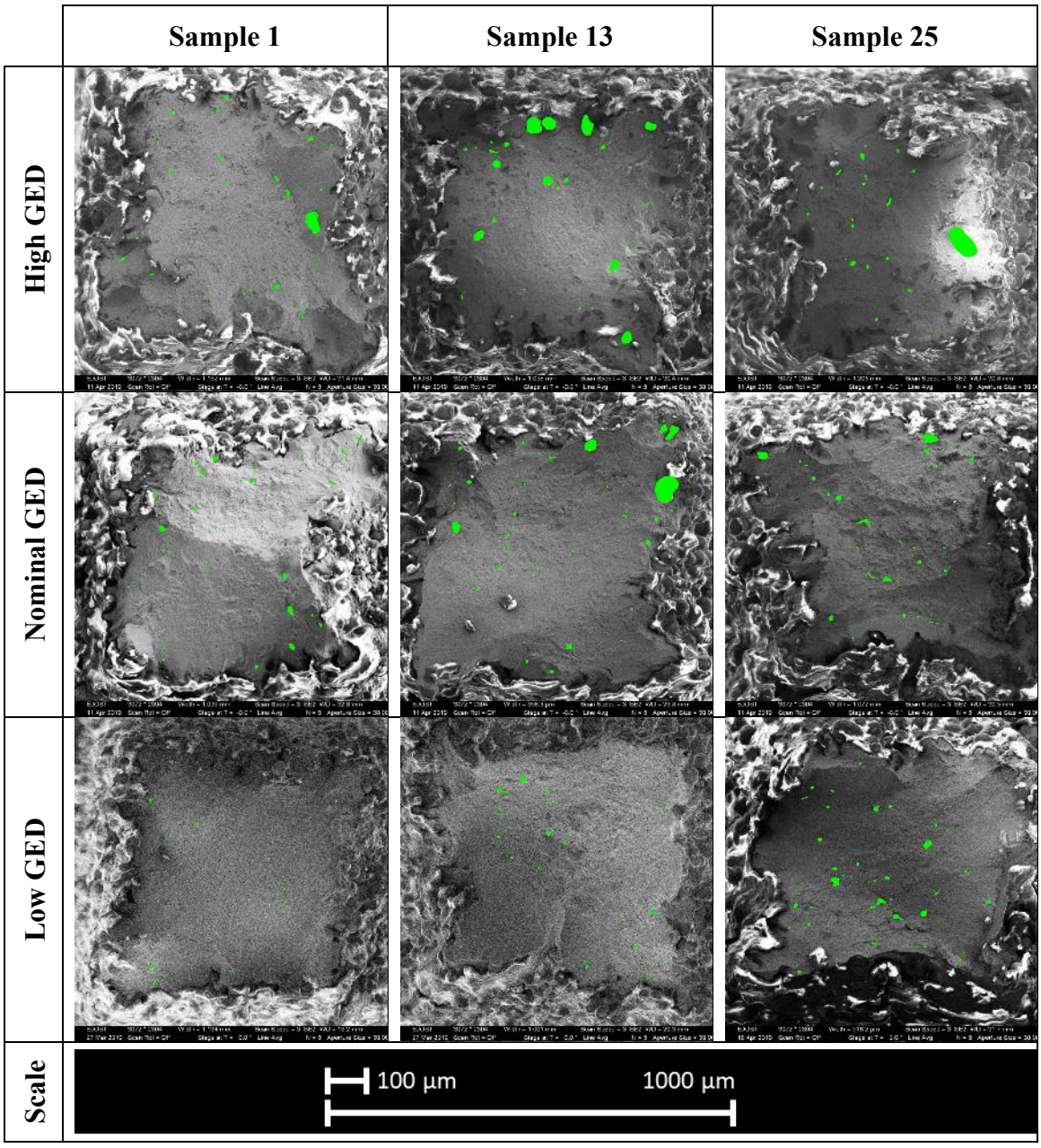

Figure 14. Select Fracture Surface SEM Images with Overlays of Identified Porosity

By using the SEM secondary detector, which detects secondary electrons and is typically used for identifying topographical information, depth can be perceived on the fracture surfaces, which tends to be vary based on the failure mode. However, SEM images alone generally only provide qualitative information and cannot quantitatively convey fracture surface topography or quantify how drastic the depth changes are without further analysis. Thus, a Zygo 3D Optical Surface Profilometer was utilized to understand the depth characteristics of the fracture surfaces. Figure 15 presents Zygo images of the same fracture surfaces as in Figure 14. In these images, the highest point on the fracture surface is shown in dark red as 0 μm and the lowest in blue at -800 μm.

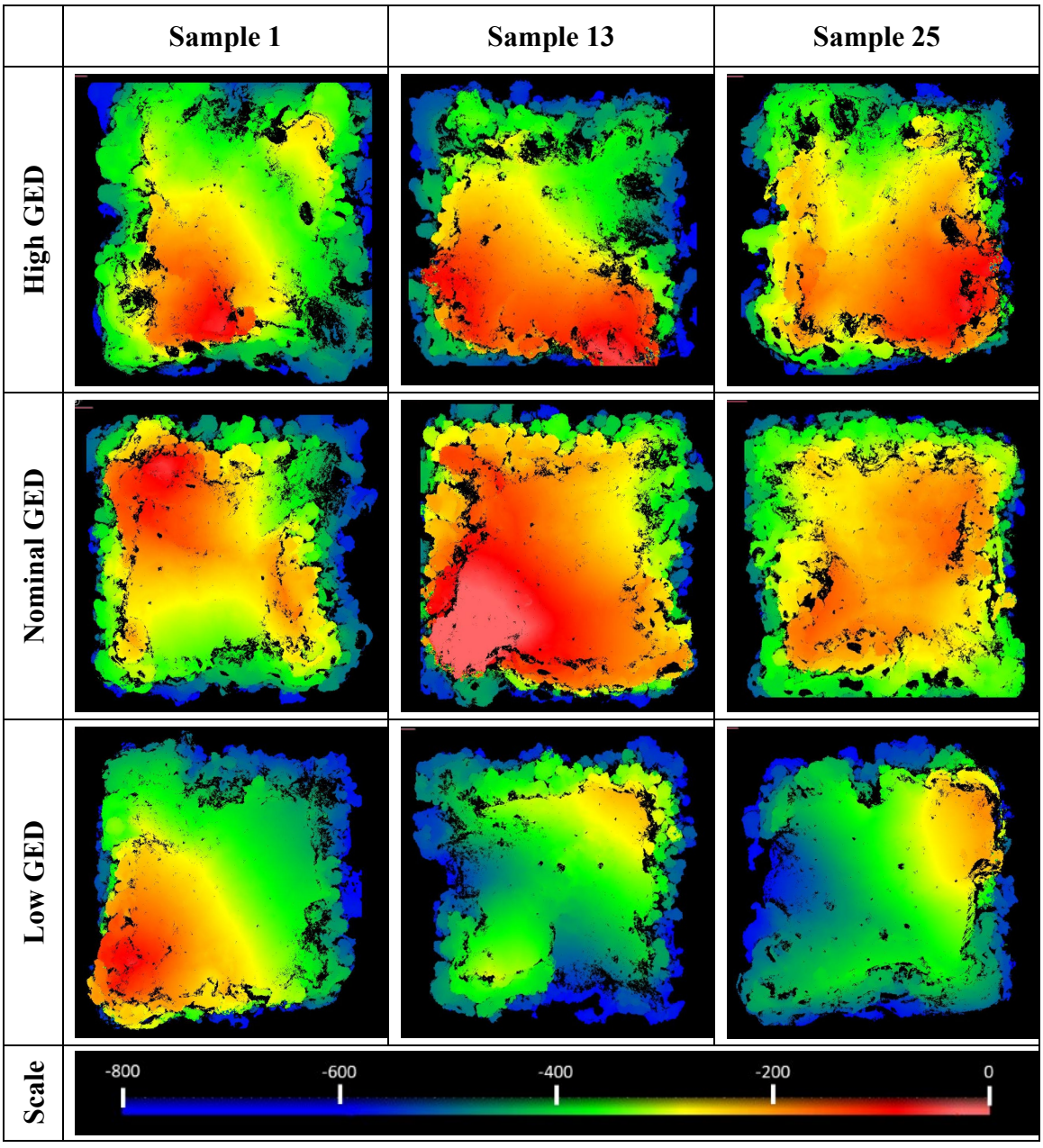

Figure 15. Select Fracture Surface Depth Maps. Black spots represent porosity.

The images presented in Figure 15 show a more accurate measurement of the fracture surface topography. From these images, cup-cone fracture surfaces can be seen, representative of ductile tensile failure. Ductile dimples in the center of the fracture surfaces, identified via SEM imaging, confirm that nearly pure tensile failure occurred in the central region of the fracture surfaces and that this failure transitioned into shear failure

on the edges of the cross sections. The low GED samples appear to be relatively flat whereas the nominal GED samples seem to have more pronounced shear lips on the fracture surfaces. However, the small sample size and lack of any obvious trend prevents definitive conclusions from being drawn based on this data.

1.11.1 SEM-Measured Porosity Characteristics

Using the ImageJ FIJI software package, quantative analysis of the fracture surfaces was performed. Porosity metrics were extracted from SEM images shown in Figure 14, where the green highlighted areas are pores identified manually. Data was organized and plotted to reveal trends in pore characteristics occurring in samples produced under different global energy density conditions.

1.11.1.1 Pore Dimensionality Parameters

First, physical characteristics of pores identified on sample fracture surfaces from SEM images will be presented. The main characteristic of porosity to be investigated is the diameter distribution. Distributions of SEM-measured pore diameter are shown in Figure 16 and are unimodal. Red vertical lines identify the mean value of pore diameter and show that mean pore value is relatively consistent across energy density samples at 0.0120 mm, 0.0111 mm, and 0.0154 mm for the high, nominal, and low GED conditions.

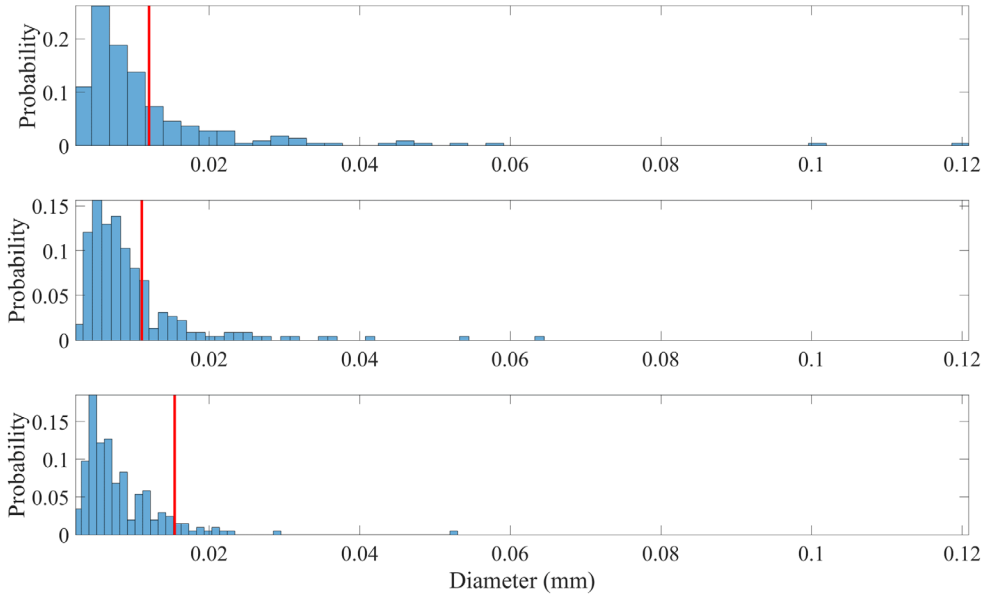

Figure 16. SEM-Measured Pore Diameter Histograms with Mean Value Shown by Vertical Line a) High GED, n=218 b) Nominal GED, n=224 c) Low GED, n=205

Table 6 presents quantitative statistics from Figure 16. Statistics shown in this table indicate that pore distribution properties in the three different print conditions are relatively consistent with respect to diameter. However, these statistical results do not consider values at the extremities of these distributions, which will be shown in the ensuing to have the greatest effect on performance.

Table 6. SEM-Measured Diameter Distribution Statistics

Values in mm^2	**Mean**	**Standard Dev.**	**Mode**
High GED	0.0120	0.0103	0.0049
Nominal GED	0.0111	0.0158	0.0049
Low GED	0.0154	0.0132	0.0042

In addition to diameter measurements, area and circularity were calculated for each individual pore detected on the fracture surface. Pore area distributions for each GED condition are shown below in Figure 17. Unsurprisingly, trends in pore area are largely

similar to the diameter distributions, with mean areas of 0.1020 mm^2, 0.1286 mm^2, and 0.2038 mm^2 for high, nominal, and low GED conditions, respectively.

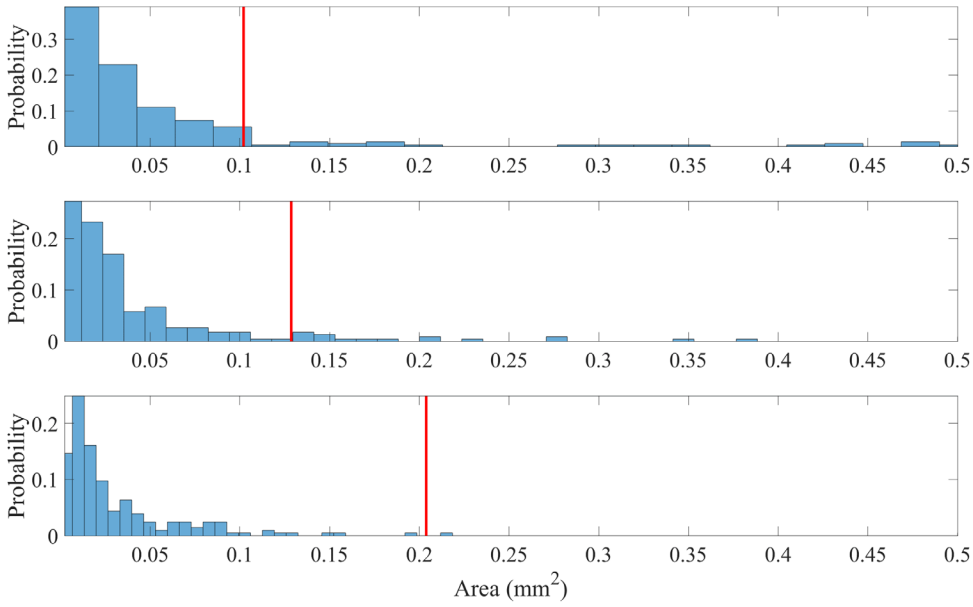

Figure 17. SEM-Measured Pore Area Histograms with Mean Value Shown by Vertical Line a) High GED, n=218 b) Nominal GED, n=224 c) Low GED, n=205

Circularity distributions are shown below in Figure 18. Circularity is defined using Equation 3

$$Circularity = \frac{4\pi A_{defect}}{P_{defect}^2} \tag{3}$$

where A is defect area and P is defect perimeter. Circularity, as the name suggests, is a quantitative metric that describes how circular an object is. Circularity is a valuable form metric to investigate, as porosity created by different mechanisms tend to have different shapes. For example, lack of fusion porosity tends to be more random in shape and orientation than gas porosity, which tends to be predominantly spherical in shape.

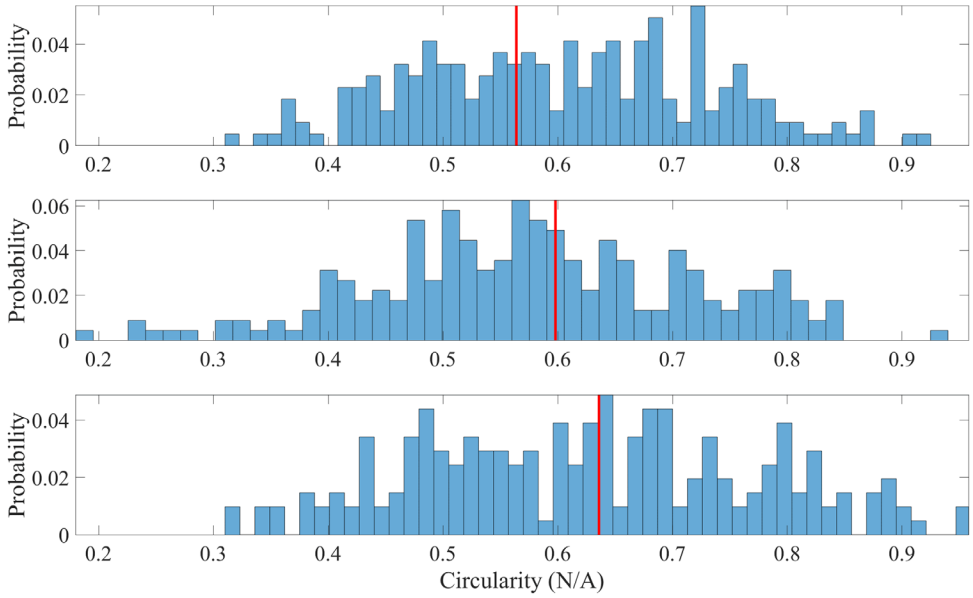

Figure 18. SEM-Measured Pore Circularity Histograms with Mean Value Shown by Vertical Line a) High GED, n=218 b) Nominal GED, n=224 c) Low GED, n=205

Circularity data presented in Figure 18 appear to be normally distributed with a wide spread or standard deviation. Additionally, circularity and GED appear to be inversely related, with high GED having relatively low circularity and low GED having relatively high circularity. One takeaway from this figure is that most pores tend to be relatively non-circular, with average pore circularity being approximately 0.6. One reason that porosity may become less circular at increasing GED values is due to the increase in keyhole pores, which often exhibit non-spherical behavior at higher energy densities, as will be discussed later in this document.

1.11.1.2 Pore Location Parameters

Using pore metric data from quantitative fractographic analysis, location data was extracted and normalized to determine if trends exist regarding pore location and energy

density. Figure 19 provides a visual representation of pore location and shows the 2D (X-Y) location of each pore for each GED type, where location (0,0) is the center of each part and encompasses the entirety of the nominal gage section of each sample. It should be noted that the circles in Figure 19 are shown for the purposes of representing the location and relative size of the pores using the pore area calculated during SEM inspection and should not be interpreted as an absolute representation of pore shape or size. Figure 19d shows the locations of pores with areas in at least the 95^{th} percentile; most of which occur near the edge of the part. Note that in the distribution of the 33 pores in this percentile range, 21 are in the high GED samples, 11 in the nominal GED, and 1 in the low GED. It is worth noting that pores are generally concentrated in the middle of the nominal edges of the gage section along the z-axis. This trend is due to necking effects from the tensile testing.

It should be noted that pores shown in Figure 19d are primarily concentrated in the upper part of the plot and may be correlated with part location on the build plate as well as the flow of the inert gas in the build chamber. This trend will be discussed further in the computed tomography inspection data sections of this document.

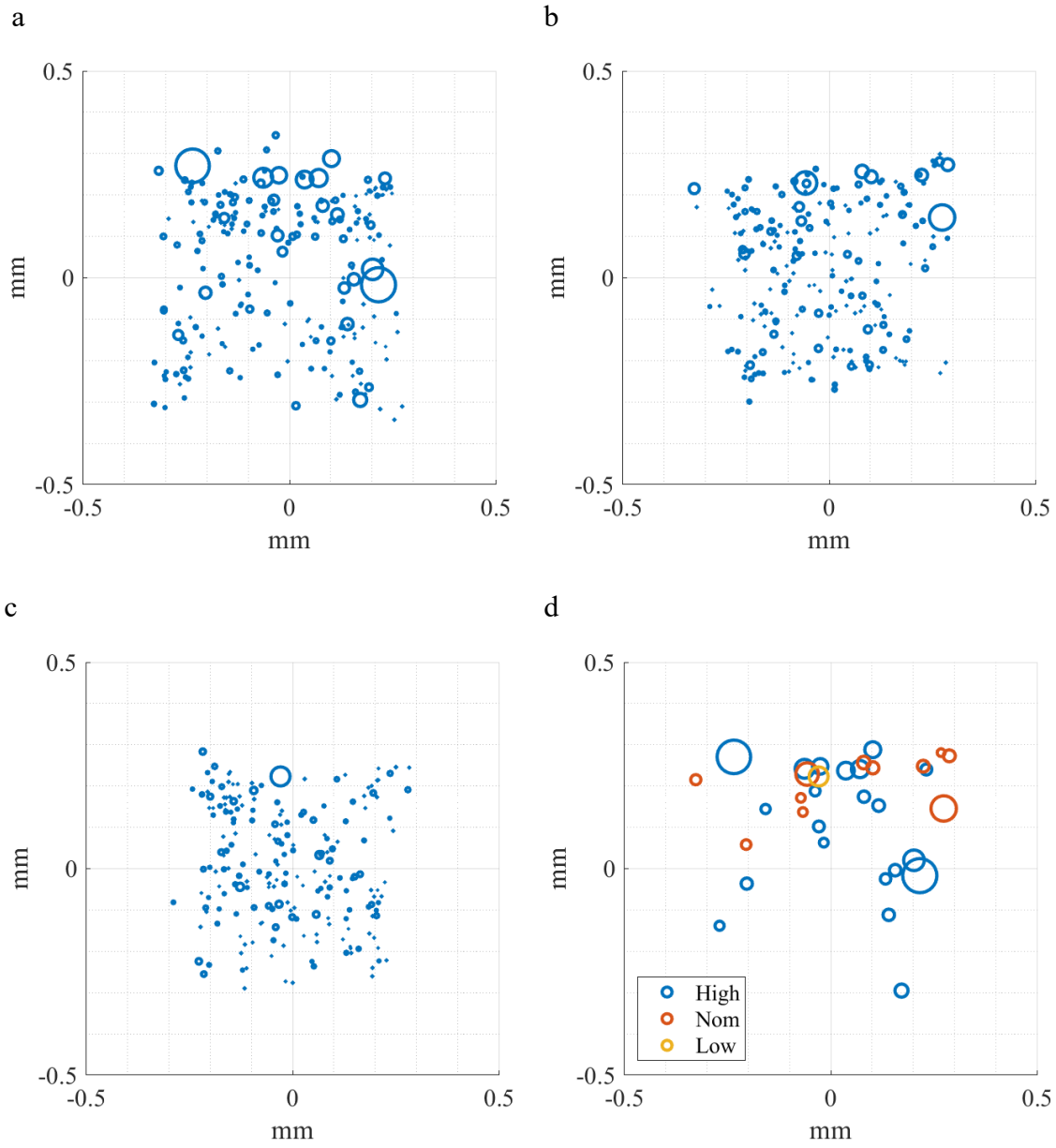

Figure 19. SEM Pore Location Mapping. a) High GED b) Nominal GED c) Low GED d) Pores in the 95th percentile or greater for all identified pores.

In addition to pore mapping, distance to center was calculated for each individual pore. This was done using Equation 4

$$D = \sqrt{[(x_{defect} - x_{gage})^2 + (y_{defect} - y_{gage})^2]} \quad (4)$$

where x_{defect} and y_{defect} are the normalized x- and y-locations of the defect as determined by defect centroid and x_{gage} and y_{gage} are the x- and y-locations of the gage section as determined by the centroid of the area bounding the fully-necked cross-section. Statistics from the distributions for pore distance to gage center are presented in Table 7.

Table 7. SEM-Measured Pore Distance to Gage Center Distribution Statistics

Values in mm	**Mean**	**Standard Dev.**
High GED	0.7599	0.1654
Nominal GED	0.7299	0.1849
Low GED	0.7350	0.1664

Table 7 shows that there is a trend that mean distance to center increases with high GED. However, data presented in Table 5 shows that ductility, which is correlated with necking behavior, is lowest in the high GED samples. Thus, SEM inspection of fracture surfaces alone is not sufficient to determine whether correlations exist between spatial energy density and pore distance to gage center. CT inspections, which were performed prior to mechanical testing and any necking behavior, will provide insight on whether these trends are true or are skewed by the variations in ductility.

1.12 Computed Tomography

CT inspections can provide three-dimensional data of the internal structure of scanned components and are commonly used for both qualitative and quantitative assessment of porosity. In this study, CT was used to provide quantitative descriptions of porosity in tensile samples prior to mechanical testing. Inspections provide significant amounts of information valuable to understanding the resultant structure of 316L components produced under varying spatial energy density conditions. Gage sections were

isolated and inspected for porosity as detailed above. Gage sections from each GED condition are shown as semi-transparent are presented in Figure 20 to visualize the identified porosity.

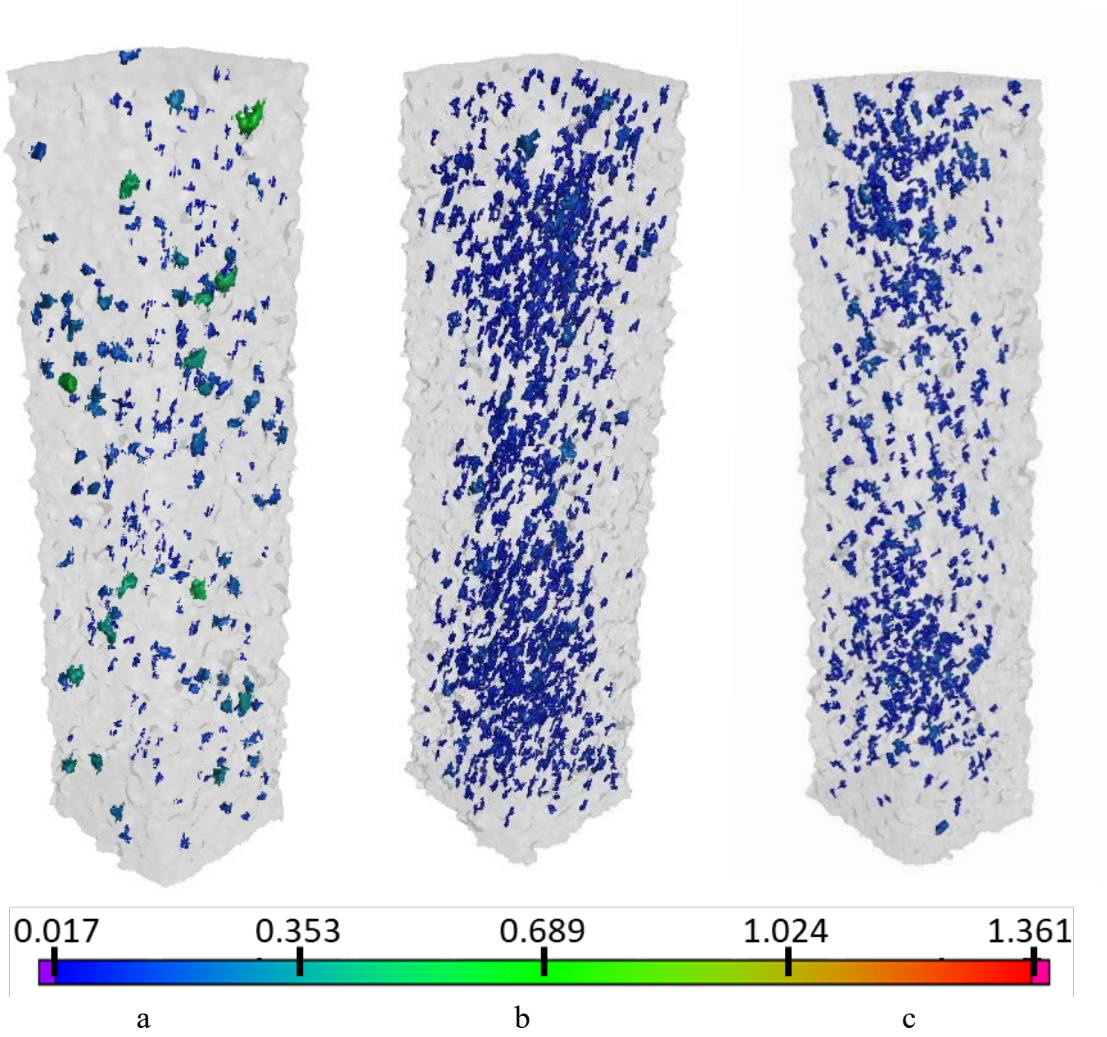

Figure 20. Semi-Transparent CT Volumes of Gage Sections in a) High b) Nominal c) Low GED Conditions. Pore color indicates volume in units of $1x10^{-3}$ mm^3.

As can be seen in Figure 20a, pores occurring in the high GED samples are generally fewer in number but much larger in size than in the nominal or low GED samples. In comparison, nominal and low GED samples seem to have a large number of pores but are of average size. Additionally, it can be generally seen in Figure 20 that pores are

uniformly spaced along the z-axis. This visual, qualitative observation is confirmed by z-position distribution data, shown in as a histogram and as a cumulative distribution function (CDF) in Figure 21.

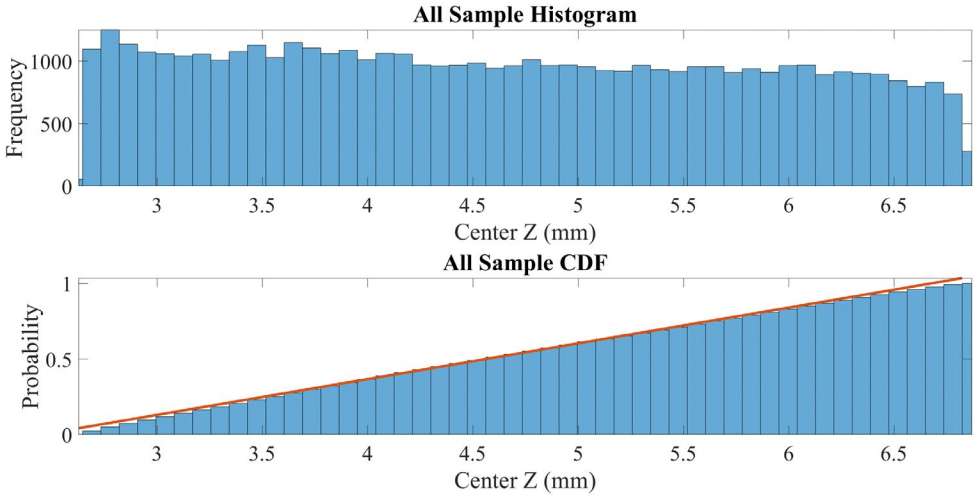

Figure 21. Histogram and Cumulative Distribution Function of Pore Centroid Z-Positions

Figure 21 shows a very uniform distribution in the top subfigure and a cumulative distribution function (CDF), which shows the cumulative probability of a pore falling at a z-position below the height denoted on the x-axis, in the lower figure. Fitting a line, shown in red, to the bin values in this lower figure, yields a r^2 correlation value of 0.999, indicating the CDF has very linear values and is thus highly uniform. This is an important point to establish, as it lends legitimacy and reliability to the quantitative SEM inspection, which essentially randomly samples porosity distributions at an arbitrary z-position. This means that assuming that the SEM inspection fracture surfaces should be representative of the entire pore distribution and is thus comparable to sampling the entire volume.

1.12.1 CT-Measured Porosity Characteristics

Quantitative pore characteristics are presented in this section similarly to SEM-measured characteristics. Compared to SEM-measured pore characteristics, those measured using CT have the added benefits of 1) a significantly larger dataset both in terms of number of pores identified and analysed as well as total number of samples inspected due to the speed of automated detection, 2) three-dimensional data which can more fully describe defects, 3) data collection prior to mechanical testing and failure, and 4) automated detection algorithms used to identify and measure porosity. Using CT inspection, 47,610 individual pores were identified across 75 samples, for an average of 635 pores per gage section. The total number of pores for each GED type is 19,542, 11,632, and 16,436 for high, nominal, and low GED. For comparison, a total of 647 pores were identified across 15 fracture surfaces using SEM inspection. Results are presented first by pore dimensionality characteristics, then by pore location trends.

1.12.1.1 Pore Dimensionality Parameters

Similar to the SEM inspections, CT inspection data was used to calculate diameter for each detected pore. Because of the larger data set collected using CT, distributions are anticipated to be much more representative of the true porosity distribution in the sample gage sections than the SEM inspections, which only analyzed the resulting fracture surface and could be skewed due to spatial nonuniformities in the porosity distributions. However, these effects should be minimal, as noted above, but not a true representation of the entire gage section. Figure 22 presents the diameter distribution of the samples from each GED condition.

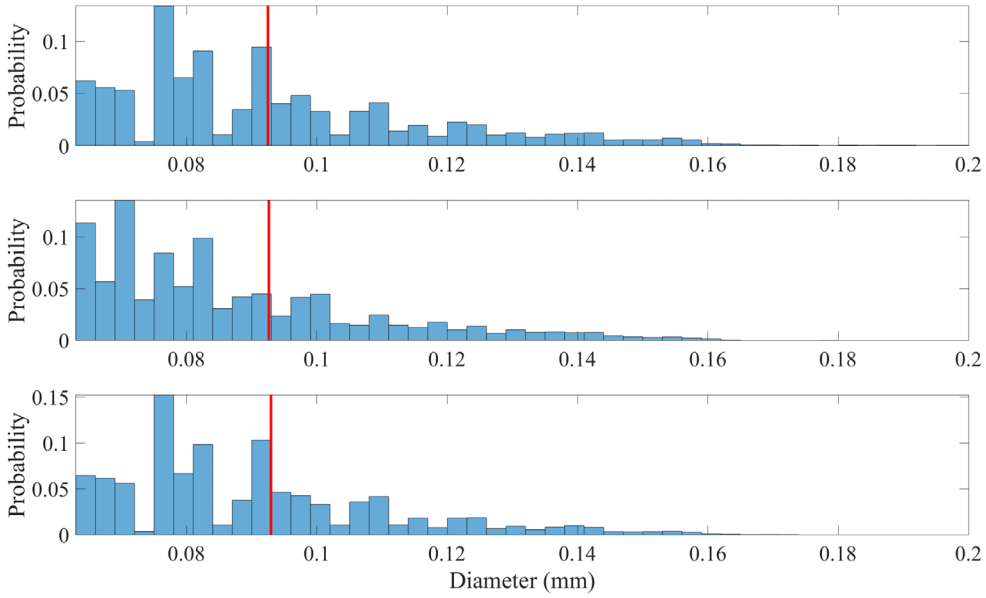

Figure 22. CT-Measured Pore Diameter Histograms with Mean Value Shown by Vertical Line a) High GED, n=19,542 b) Nominal GED, n=11,632 c) Low GED, n=16,436

As with diameter distributions from SEM inspections, mean, standard deviation, and mode values for the distributions were calculated and are consistent across the tested energy density conditions. These statistics are presented in Table 8. However, these statistics are not fully descriptive of the porosity diameter distributions, as they provide no information about the differences in the largest pores in these samples, which will be shown to have the most significant impact on mechanical behavior. Additionally, pore volume can be measured using the 3D data obtained from computed tomography. Distributions of this data are presented in Figure 23.

Table 8. CT-Measured Diameter Distribution Statistics

Values in mm^2	**Mean**	**Standard Dev.**	**Mode**
High GED	0.0925	0.0242	0.0770
Nominal GED	0.0926	0.0231	0.0690
Low GED	0.0929	0.0227	0.0770

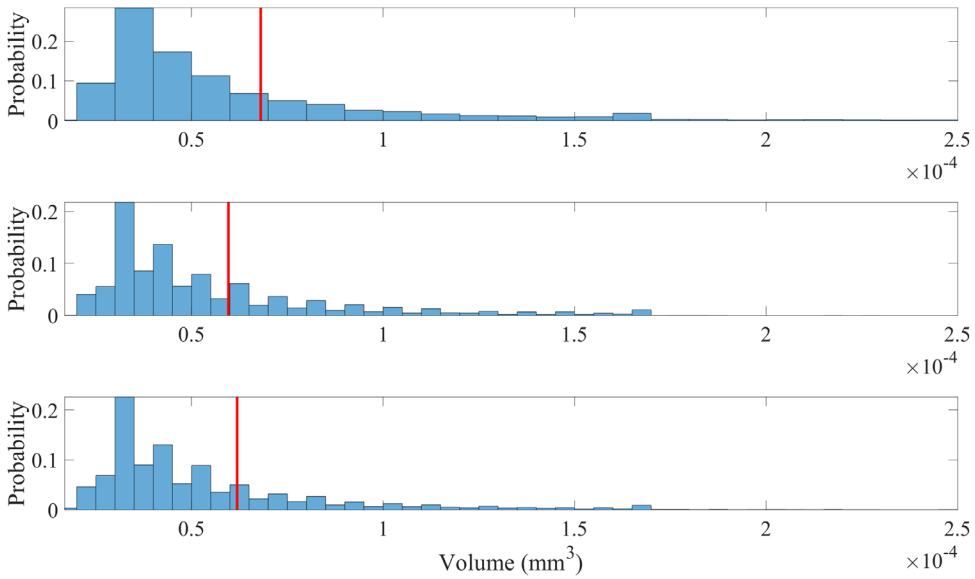

Figure 23. CT-Measured Pore Volume Histograms with Mean Value Shown by Vertical Line a) High GED, n=19,542 b) Nominal GED, n=11,632 c) Low GED, n=16,436

While there is slight variation between the mean values of $0.681x10^{-4}$ mm^3, $0.596x10^{-4}$ mm^3, and $0.619x10^{-4}$ mm^3 in the high, nominal, and low GED conditions, the distributions are largely similar. Once again, this consistency indicates that, in general, the porosity distributions are relatively similar across the energy density conditions for most pores. However, it will be shown that the largest pores existing on the extremes dominate mechanical performance and can be used as more reliable performance predictors than total pore distributions.

Table 9. CT-Measured Volume Distribution Statistics

Values in $1x10^{-4}$ mm^3	**Mean**	**Standard Dev.**	**Mode**
High GED	0.681	0.784	0.304
Nominal GED	0.596	0.556	0.304
Low GED	0.619	0.513	0.304

In addition to porosity size metrics, shape descriptors were considered to further understand the porosity contained in the analyzed samples. Compactness is one shape metric that can be used to classify porosity type and is the ratio of the pore volume to the volume of a circumscribed sphere. A spherical defect would have a percent compactness value of 1.0 whereas an elongated, ellipsoidal defect would have a lower compactness value. Mathematically, compactness can be described using Equation 5

$$Compactness = \frac{V_{defect}}{V_{sphere}} = \frac{6V_{defect}}{\pi d_{defect}^3} \tag{5}$$

where V_{defect} is the volume of the defect of interest and d_{defect} is the maximum diameter of the defect. Compactness distributions are shown below in Figure 24. As can be seen in Figure 24, the high GED distribution has the highest mean value, as indicated by the red, vertical line. However, the high GED distribution also shows that there are a significant number of pores were compactness values in the range of [0, 0.125]. This indicates that a high percentage of pores in the high GED samples are elongated or non-normal in shape.

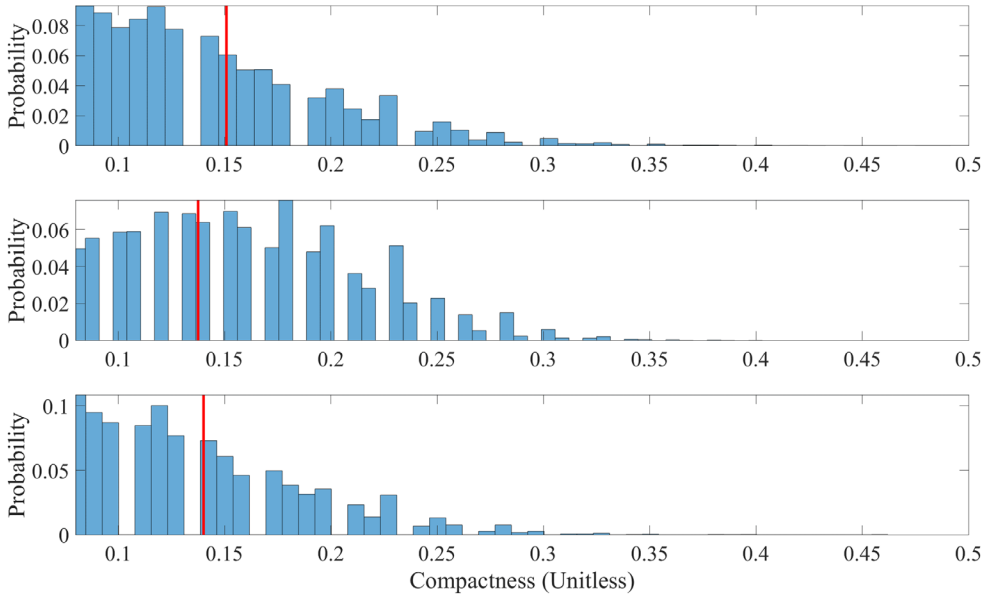

Figure 24. CT-Measured Pore Compactness Histograms with Mean Value Shown by Vertical Line a) High GED, n=19,542 b) Nominal GED, n=11,632 c) Low GED, n=16,436

Sphericity is another metric that can be used to describe pore shape and specifies the ratio between the surface of a sphere with the same volume as the defect and the surface area of the defect. Equation 6 describes sphericity mathematically

$$Sphericity = \frac{A_{sphere}}{A_{defect}} = \frac{\pi d^2}{A_{defect}} \tag{6}$$

where A_{defect} is the surface area of the defect and d is the diameter of the equivalent sphere. Sphericity distributions for each GED condition are presented in Figure 25. This figure shows that the mean value of sphericity is very similar for each GED condition at 0.548, 0.551, and 0.551. Additionally, this figure shows that these distributions are nearly identical across conditions.

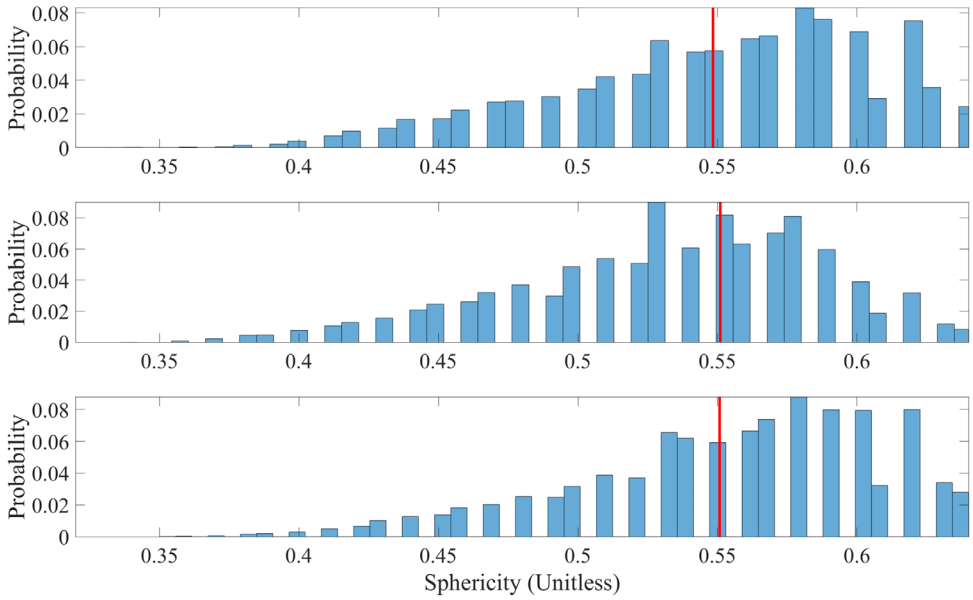

Figure 25. CT-Measured Pore Sphericity Histograms with Mean Value Shown by Vertical Line a) High GED, n=19,542 b) Nominal GED, n=11,632 c) Low GED, n=16,436

1.12.1.2 Pore Location Parameters

Using CT pore location data, X-Y location was extracted for each pore based on its centroid. Equation 4 was used to normalize the X- and Y-locations of each defect

$$P_{defect} - P_{Gage\ Center} \tag{7}$$

where P_{defect} and $P_{Gage\ Center}$ are the x- or y-positional data of a pore and the gage center. $P_{Gage\ Center}$ was specified for each sample using the CAD model of the tensile sample array. Figure 26 shows normalized location maps of pores organized by GED type and volumetric percentile of all analyzed pores. For example, the top map in the high GED column shows pore location data for pores between the 0^{th} and 25^{th} percentile, inclusive.

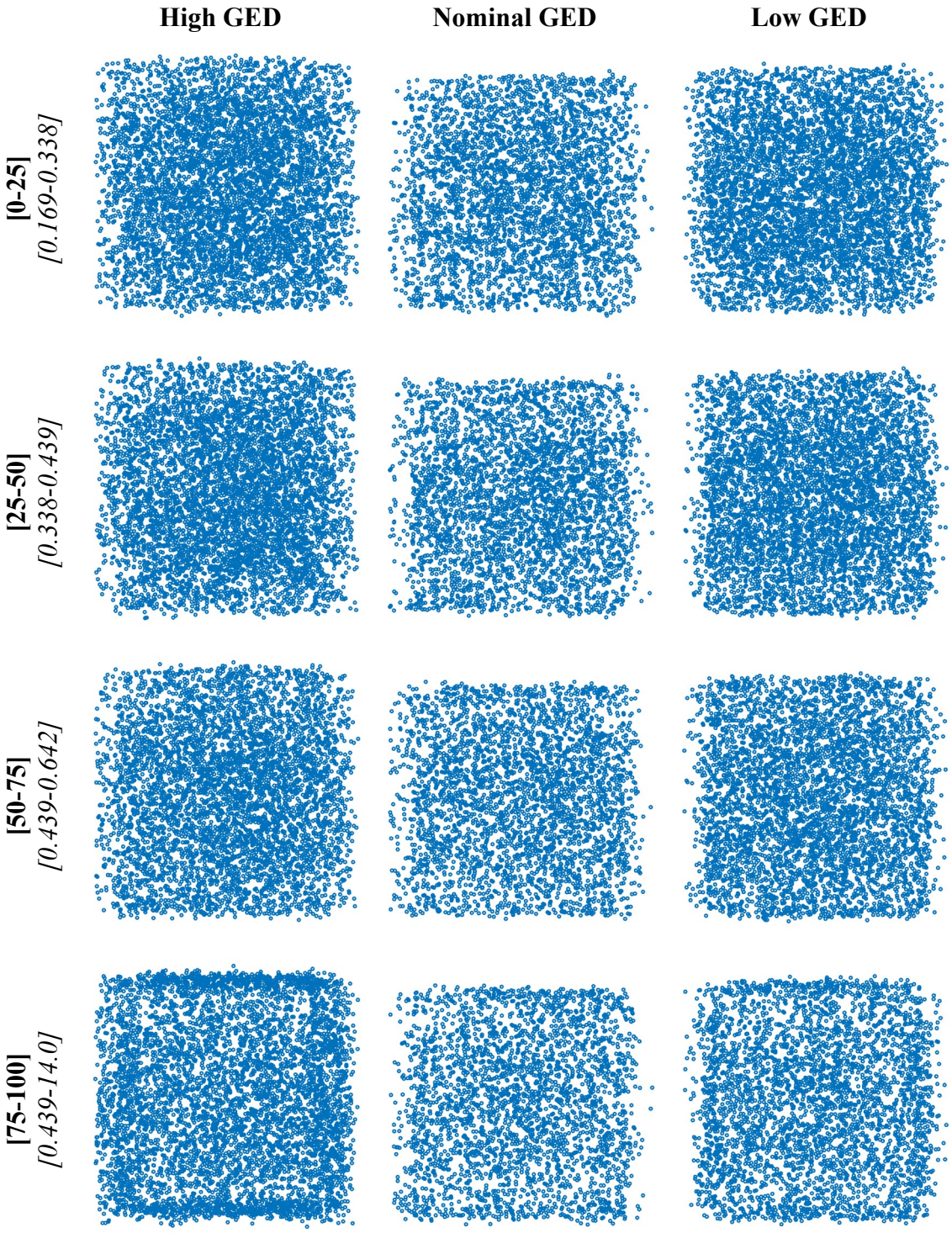
High GED
Nominal GED
Low GED
[0-25]
[0.169-0.338]
[25-50]
[0.338-0.439]
[50-75]
[0.439-0.642]
[75-100]
[0.439-14.0]

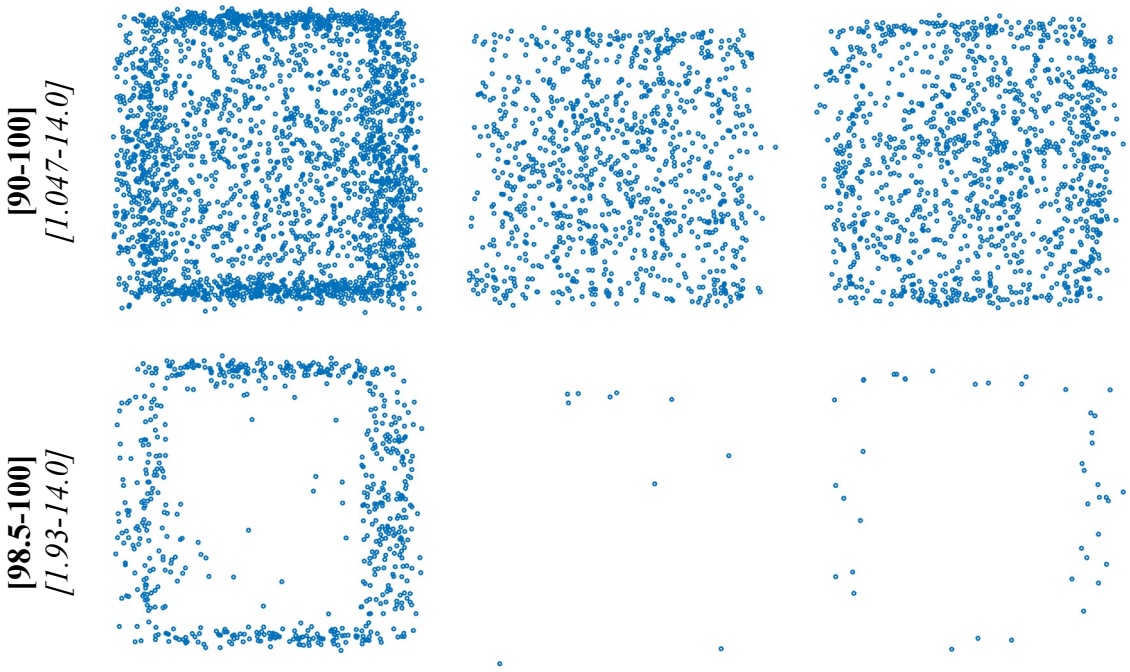

Figure 26. Pore location maps at uniform scaling for various percentiles for each GED condition. Bold bracketed numbers in leftmost column indicate percentile value. Volume values are shown in italics in units of $1x10^{-4}$ mm^3.

Not much information can be garnered from looking at the maps in Figure 26 showing pores below the 75th percentile except that the distributions seem to be largely uniform along the x-y plane. However, a trend begins to emerge in the high GED maps looking at the location maps for the [75-100], [90-100], and [98.5-100] ranges. In these subfigures there begins to be a concentration of porosity around the edge of the sample. This trend becomes clearest in the [98.5-100] range in which nearly all of the pores in this range are on the outside edge of the sample. Quantitatively, 673, 10, and 43 pores exist in this range on the high, nominal, and low GED samples, respectively, highlighting how prevalent this trend is in the high GED samples. Figure 27 presents histograms of the distance to gage center of each pore shown in the corresponding subfigures of Figure 26. The data in this histogram was calculated using Equation 4 as with the SEM data.

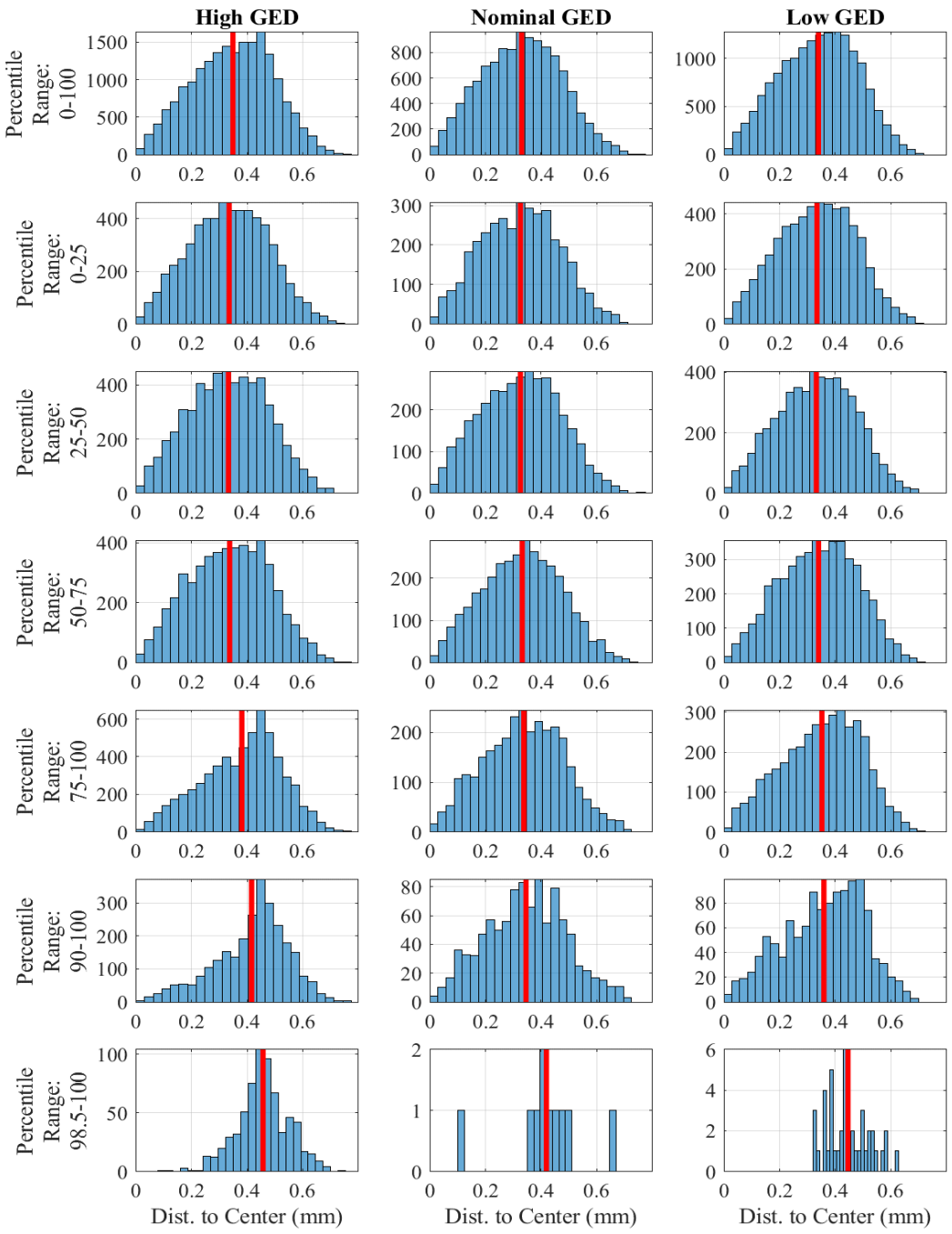

Figure 27. Histograms of Pore Distance to Gage Center at Various Volumetric Percentile Ranges

The mean value of pore distance to gage center for the high GED subfigures of Figure 27 increased as pore volume increased. These mean values are presented in Table

10, in which this trend can be seen more clearly. Average pore distance to gage center for all pores is nearly the same across GED conditions at 0.349 mm, 0.343 mm, and 0.343 mm for high, nominal, and low GED. However, there is a significant difference when only considered the largest pores at 0.457 mm, 0.352 mm, 0.3535 mm for high, nominal, and low GED conditions.

Table 10. Mean Value of Histograms of Pore Distance to Gage Center at Various Volumetric Percentile Ranges

Percentile Range	High GED	Nominal GED	Low GED
All Pores: 0-100	0.349	0.343	0.343
0-25	0.336	0.343	0.345
25-50	0.333	0.343	0.344
50-75	0.337	0.340	0.340
75-100	0.381	0.346	0.346
90-100	0.416	0.352	0.346
98.5-100	0.457	0.352	0.353

To better understand the role of porosity defects, innate to the LPBF AM process, on 316L SS tensile performance, linear regressions were performed to correlate porosity metrics and mechanical performance measures of interest. Correlations were calculated using the linear least squares regression method, which fits a line to data points by minimizing the error between the fit curve and the raw data as shown in Equation 8,

$$\min \sum_{i=1}^{n} [y_i - f(x_i)]^2 \tag{8}$$

where n is the number of data points, y_i is the value of the i^{th} point of the raw data, and $f(x_i)$ is the value of the line of best fit at the x_i. This method of relationship quantification was chosen because it allows for comparison between the 100+ relationships examined in this study. More complex relational fits such as quadratic could mask relationships and

make it more difficult to isolate porosity characteristics that strongly influence mechanical behavior. Additionally, linear least squares is computationally efficient and easy to interpret using the coefficient of determination (COD), r^2. This value makes comparison between relationships fair and easy to identify. COD is defined in Equation 9, Equation 10, and Equation 11,

$$S_t = \sum_{i=1}^{n} [y_i - f(x_i)]^2 \tag{9}$$

$$S_r = \sum_{i=1}^{n} [y_i - \overline{y_i}]^2 \tag{10}$$

$$r^2 = \frac{S_t - S_r}{S_t} \tag{11}$$

where $\overline{y_i}$ is the average of the y_i values, S_t is the total sum of squares, and S_r is the residual sum of squares. Coefficient of determination results can be interpreted as how well the fit line does when compared to choosing the mean value of a distribution. In other words, 1.0 reflects a line that is fit perfectly to raw data and using it to estimate the value, y_i, of a data point, x_i, will yield exact results. A value of 0 would mean that using the fit line is equally good to using the mean value, $\overline{y_i}$ as the estimate, and a negative value means that using the line is worse than using the mean value.

Correlation results will be presented first using SEM inspection results followed by CT inspection results. Relationship results calculated using the two methods will then be compared to assess the relative fidelity of these methods. Two cases were considered

wherein: (1) the mean value of the porosity metric for a sample was calculated by averaging that metric for all pores in a sample and (2) mean value of the porosity metric for pores larger than 150 μm in diameter was used. This 150 μm threshold was chosen because it only considers the largest pores, which are hypothesized to have a dominating effect on performance. Additionally, the size of these pores makes measurements of shape and size less distorted by the voxelized nature of CT inspections. Additionally, stronger relationships that may exist between larger pores and performance are useful for establishing inspection parameters for eventual qualification.

1.12.2 SEM-Correlations

Using porosity measurement metrics gathered using quantitative SEM inspection, relationships were made between these porosity and tensile performance. Figure 28 shows COD results for the analysis considering all pores in a sample. Results are presented as a heatmap in which the r^2 value is shown as well as represented by a color scale. In this way, the strongest relationships of the 114 calculated using SEM data can be easily discerned. As can be seen in this figure, consistently strong correlations exist between porosity metrics involving pore size such as area, bounding box size, major and minor diameters, and maximum diameter and cross-sectional area. Additionally, results in Figure 28 suggest that, in general, little to no correlation exists between porosity and ultimate tensile strength or modulus.

Results presented in Figure 28 do suggest a relationship between porosity and ductility. Specifically, a *relatively* strong correlation of 0.40 exists between major diameter and ductility. Bounding box height and major elliptical diameter have similar correlation

strengths with ductility and UTS strain, likely due to the similarity in these characteristics. The difference in bounding box height vs bounding box width correlation strengths of 0.55 vs 0.20 for UTS strain and 0.48 vs 0.19 for ductility may be indicative of a preferential direction porosity orientation parallel to the y-axis of the part as defined using the coordinate system in Figure 4, however further studies would need to be performed to adequately assess this effect. A relatively strong correlation of 0.59 exists between average pore distance to gage center and ductility. However, as mentioned before, SEM inspections were performed post-fracture, which means that necking was not accounted for in these results. Computed tomography results, taken prior to mechanical testing, will provide a more accurate picture of the true relationship between these two parameters. Interestingly, circularity, a measurement of pore shape, displays no correlation with any mechanical property measured. Pores in excess of the 150 μm threshold were not specifically isolated for correlation in the SEM dataset due to the small sample size of these datasets. Several samples, specifically in the nominal and low GED conditions did not have adequate numbers of pores in excess of this size, making correlations unreliable and thus not a fair comparison to the results in Figure 28.

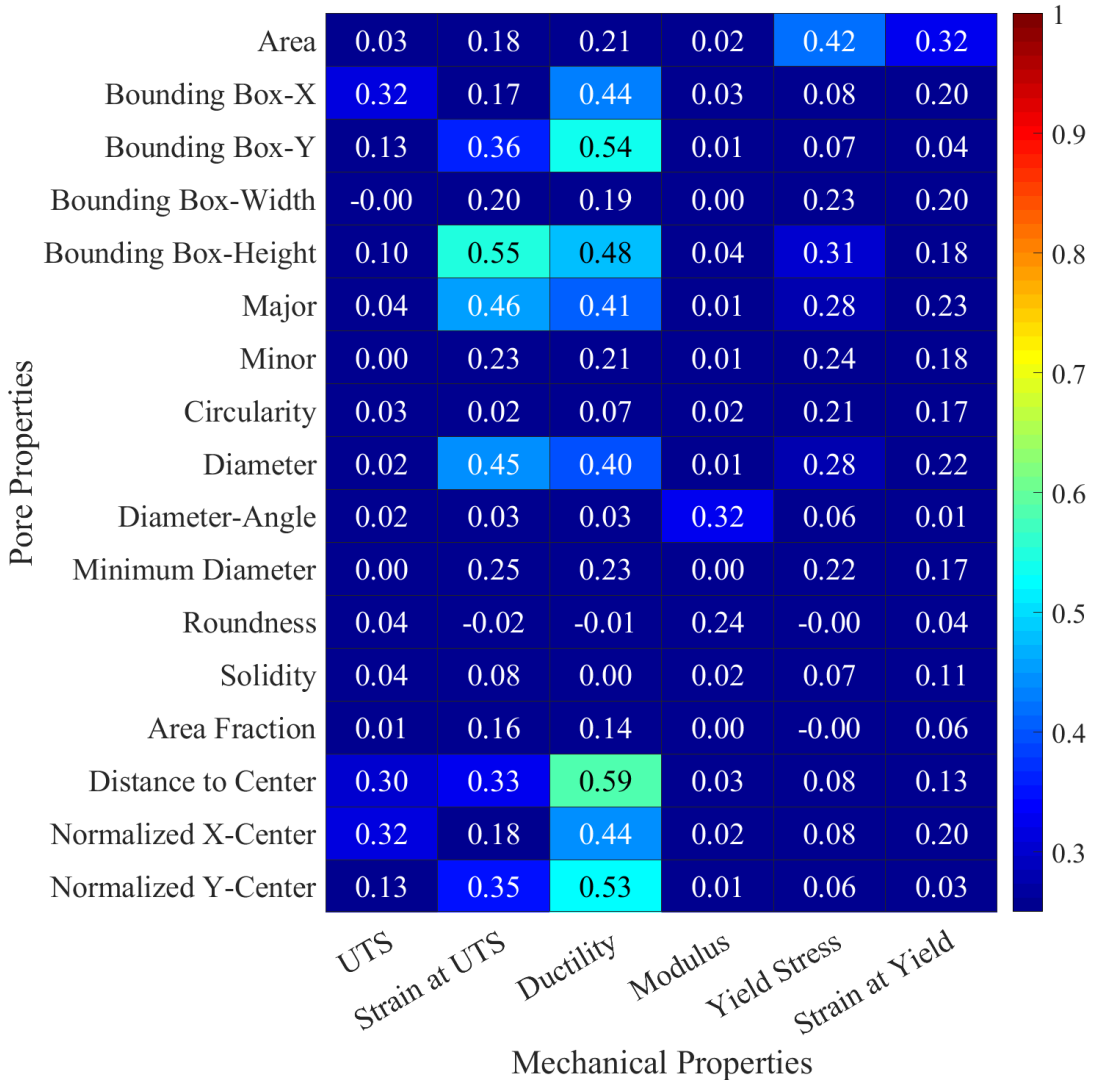

Figure 28. SEM: All Pores Considered Linear Regression R^2 Values Correlating Pore and Mechanical Properties. Colors Indicate Value Between 0.3 and 1.0

1.12.3 CT-Correlations

Similar to SEM-Correlation results presented in the previous sub-section, CT results were correlated with mechanical properties and are presented in the following figures as heatmaps. Figure 29 presents results of porosity metric correlations and mechanical properties in which all pores were used to calculate porosity metrics for each

sample. Using CT results, correlations are again seen with ductility. COD values in the range of 0.32-0.48 are similar to SEM results for various porosity metrics vs ductility. Porosity metrics such as probability, diameter, volume, and surface area, are all moderately correlated with ductility, having COD values in the aforementioned range. However, pore distance to gage center as measured using CT, which is done prior to mechanical testing and thus does not include any necking effects, has no statistical correlation with an r^2 value of -0.02. This lack of relationship is contradictory to results observed in the SEM-Correlations section and may indicate SEM results were altered by necking behavior. Shape descriptors such as compactness and sphericity have little to no correlation with mechanical properties other than modulus.

Yield stress and yield strain exhibit no correlation with any porosity metrics measured in this study. Modulus, however, shows correlation with compactness, sphericity, project size y, PCA Deviation 3, and minimum PCA deviation ratio, having relation values of 0.35, 0.29, 0.41, 0.37, and 0.39, respectively. Shape descriptors such as compactness and sphericity have little to no correlation with mechanical properties other than modulus and are thus generally poor predicators of material behavior. This is consistent with SEM results, which also indicated little to no relationship between pore shape and tensile performance.

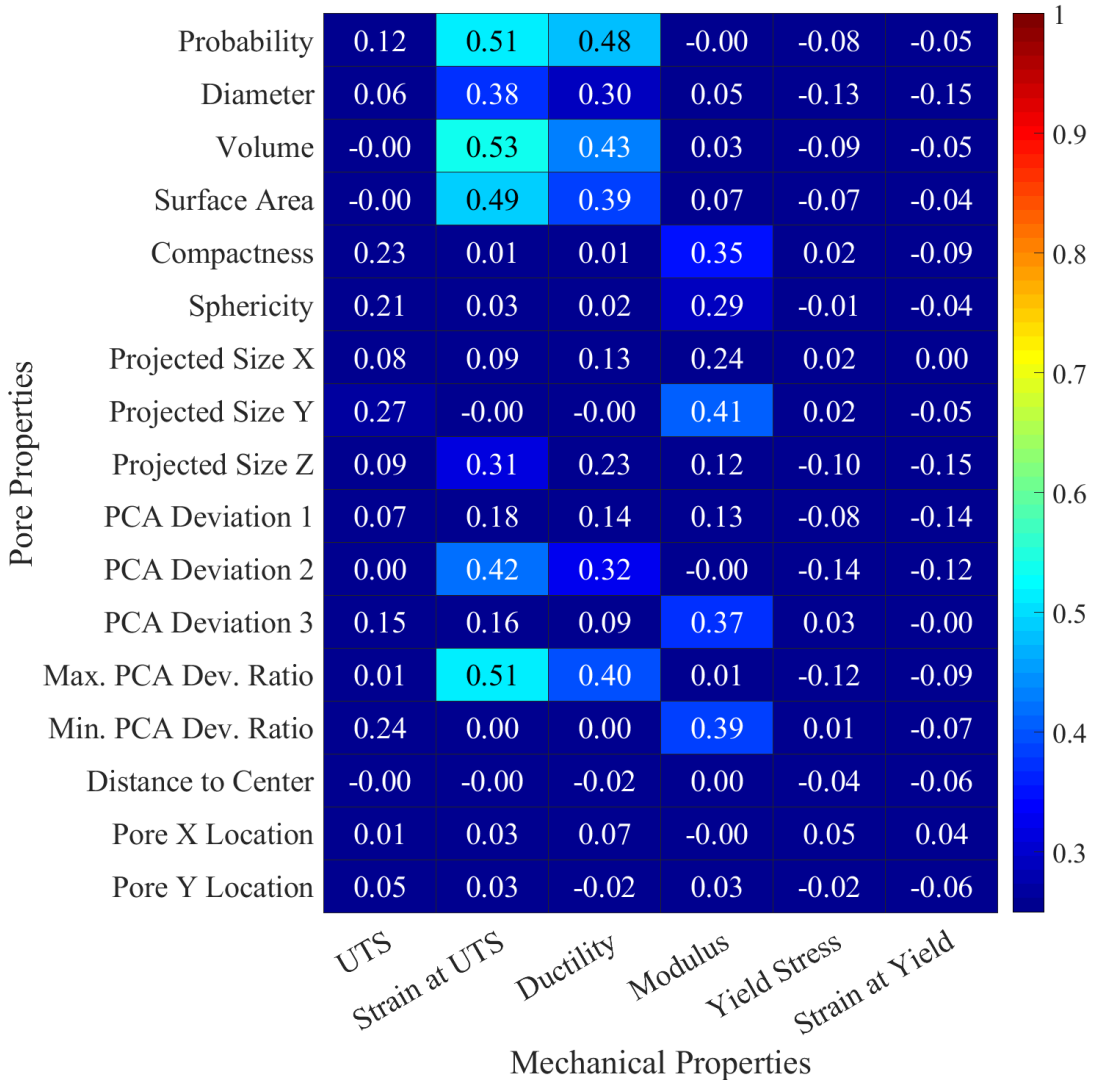

Figure 29. CT: All Pores Considered Linear Regression R^2 Values Correlating Pore and Mechanical Properties. Colors Indicate Value Between 0.3 and 1.0

Despite relationships existing between porosity metrics and mechanical properties when considering all detected pores, relationships are relatively weak and thus not particularly useful for serving as inspection criterion, having a maximum COD of 0.53 for volume vs strain at UTS. With such low CODs, these relationships provide relatively little value for predicting the performance of a part on the basis of porosity descriptors.

However, consideration of only pores > 150 μm in diameter produces significantly stronger COD values. These relationships are presented in Figure 30 while improvements measured as differences between the two cases are presented in Figure 31. Figure 32 presents the percent decrease in mechanical property as a function of porosity characteristic.Furtherore, This value was calculated by dividing the range of mechanical performance values obtained using the fitted trend line by the highest mechanical performance value. Strong relationships are presented in this figure, however consideration of the correlation strength presented in Figure 30 and Figure 31 is needed to properly interpret this figure.

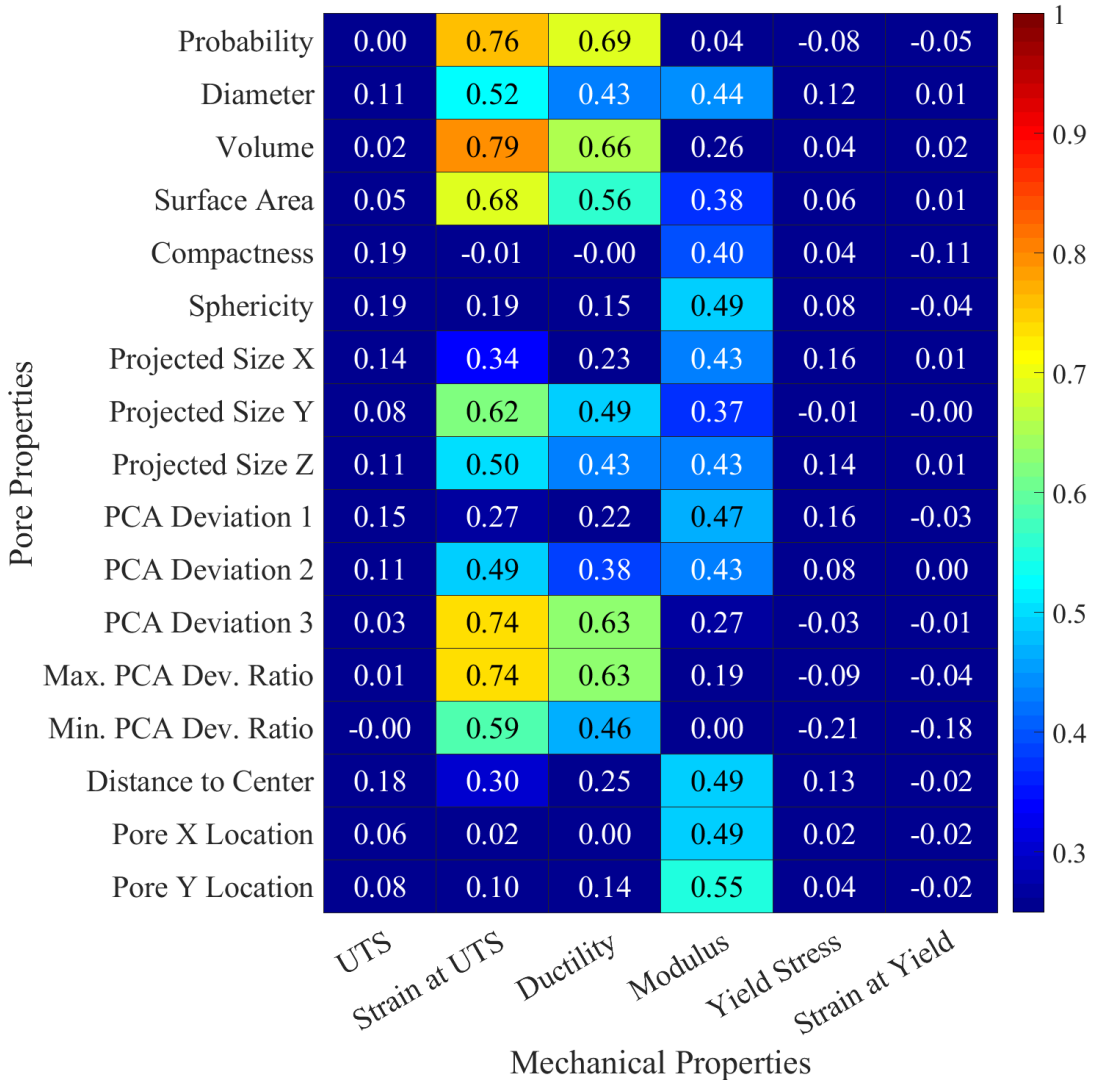

Figure 30. CT: Pores > 150 µm in Diameter Considered Linear Regression R^2 Values Correlating Pore and Mechanical Properties. Colors Indicate Value Between 0.3 and 1.0

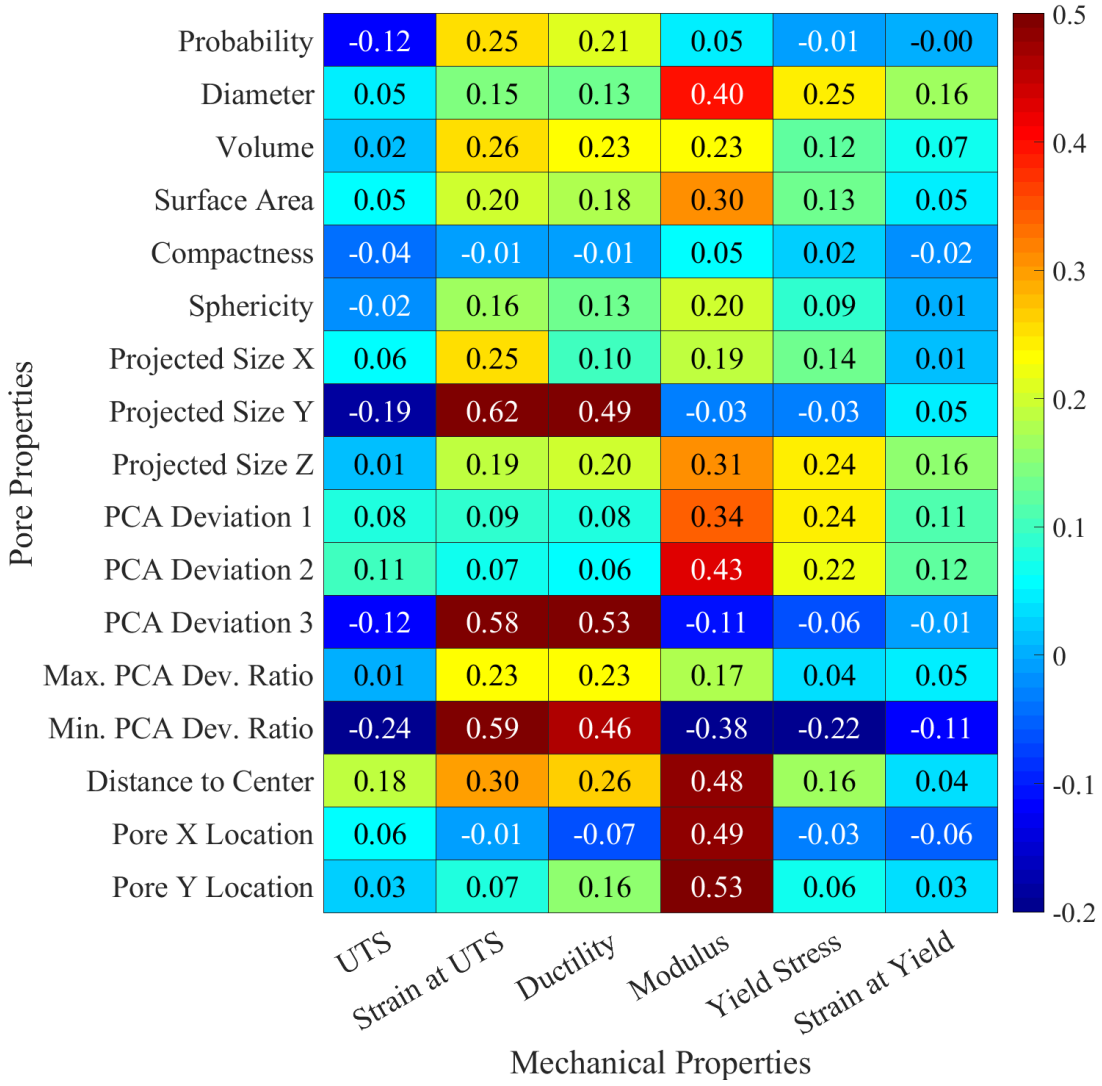

Figure 31. CT: R^2 Improvement When Considering Only Pores > 150 µm in Diameter

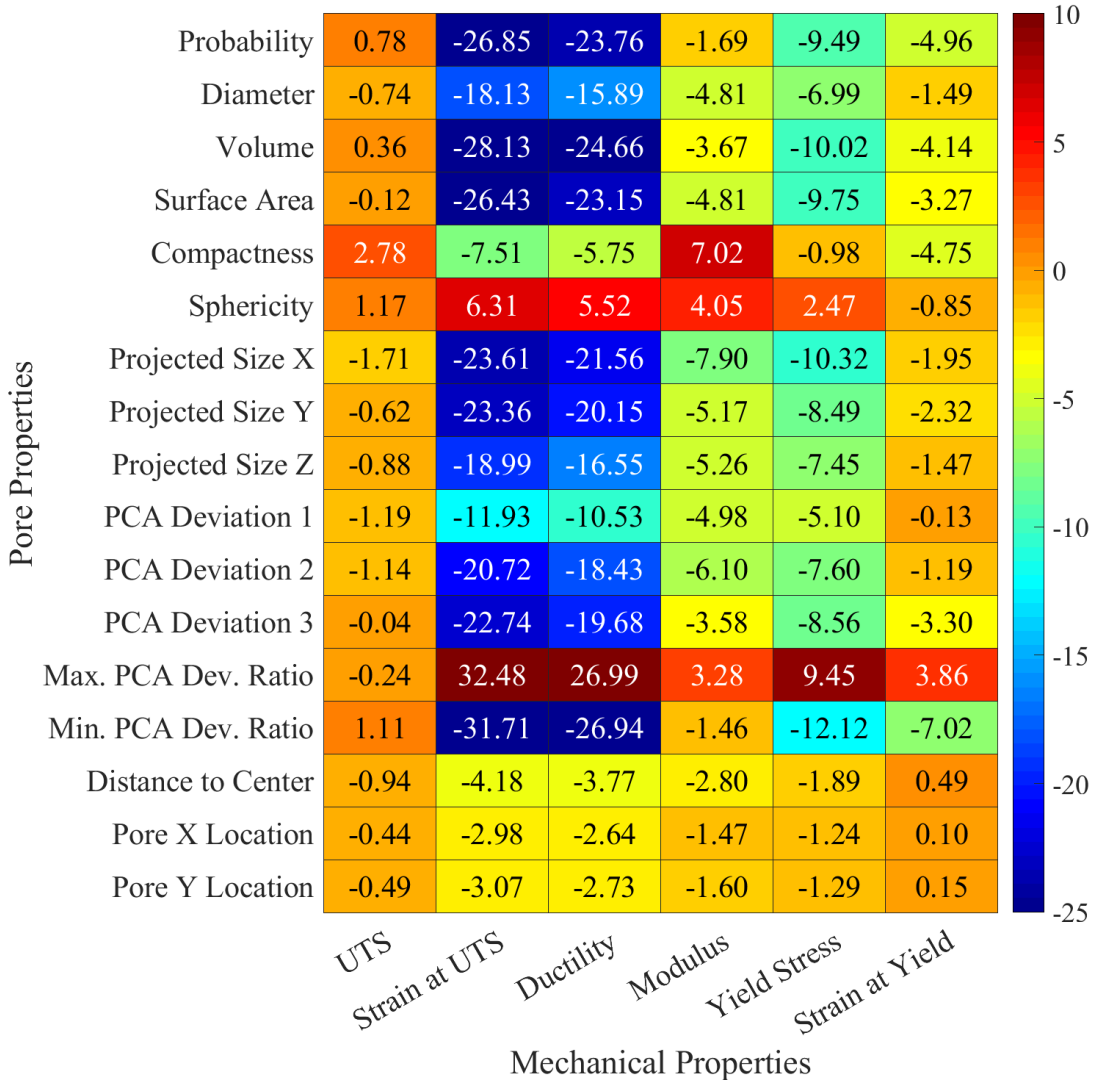

Figure 32. CT: Percent Range in Mechanical Property Calculated Using Pores > 150 µm in Diameter Trend Lines.

As shown above, consideration of only the largest pores in a sample, those over 150 µm in diameter, serves as a significantly better predictor of performance than does consideration of all pores. In general, relationships that were already strong were shown as strengthened by using this method. Specifically, probability as well as size descriptors such as diameter, volume, surface area, and projected size, increased significantly for ductility and strain at UTS. Pore volume continues to be one of the best indicators for strain at UTS

and ductility performance, having COD values of 0.79 and 0.66, respectively. Probability gives similar COD values for these performance metrics at 0.76 and 0.69. However, probability (as reported here) is calculated using a proprietary algorithm on an undefined scale and is thus more difficult to understand or transfer to other systems. Additionally, pore volume provides better prediction of performance.

Figure 32 shows that nearly all correlations observed between pores and mechanical properties is one of decreasing mechanical property with increasing porosity characteristic. Most useful from this chart is that probability and volume, two of the best identified predictors of tensile behavior in this study, show decreases of strain at UTS and ductility properties of 23-30%. The significant decreases in performance are indicative of the severity of the effects of porosity on mechanical performance.

1.13 Discussion of Results

The data presented in this study provide promising results for the future of additively manufactured 316L stainless steel components subject to tensile loading conditions, specifically concerning the establishment of qualification metrics and inspection thresholds. The focus of this section will be: 1) trends regarding the existence of keyhole porosity and its relationship with global energy density and 2) porosity metric correlations with tensile performance and their implications for qualification inspections. Additionally, the results in this study will be compared to those of previous studies.

1.13.1 Keyhole Porosity

Location maps generated from computed tomography data shown in Figure 26 highlight trends relating pore volume and location. From the subfigures showing location of pores in the [90-100] and [98.5-100] ranges of volumetric percentiles, it is clear that the largest pores tend to form around the sample edges. It is hypothesized that the cause of the significant increase in distance to gage center of the largest pores is due to the path of the laser during part buildup. It is well-established that the likelihood of keyhole porosity formation is increased due to excessive energy input in LPBF AM and similar processes such as laser welding [28–30]. It is plausible that the raster pattern used in the printing of the samples of interest resulted in non-uniform energy density input, specifically a localized increase in spatial energy density around the edge of the samples. The instantaneous zero-velocity of the laser as it reverses directions at the edges of samples causes a spike in local energy density, resulting in conditions ideal for the formation of keyhole porosity. Based on these results, it seems that even higher GED input would result in keyhole porosity forming not only at the edges of samples but in the center of these samples as well, resulting in further reduction of tensile properties. Figure 33 presents images of the same keyhole pore at different magnifications as seen from the processed CT volume. These images highlight both the location of the pore as close to the edge of the sample as well as the generally non-spherical shape of the defect.

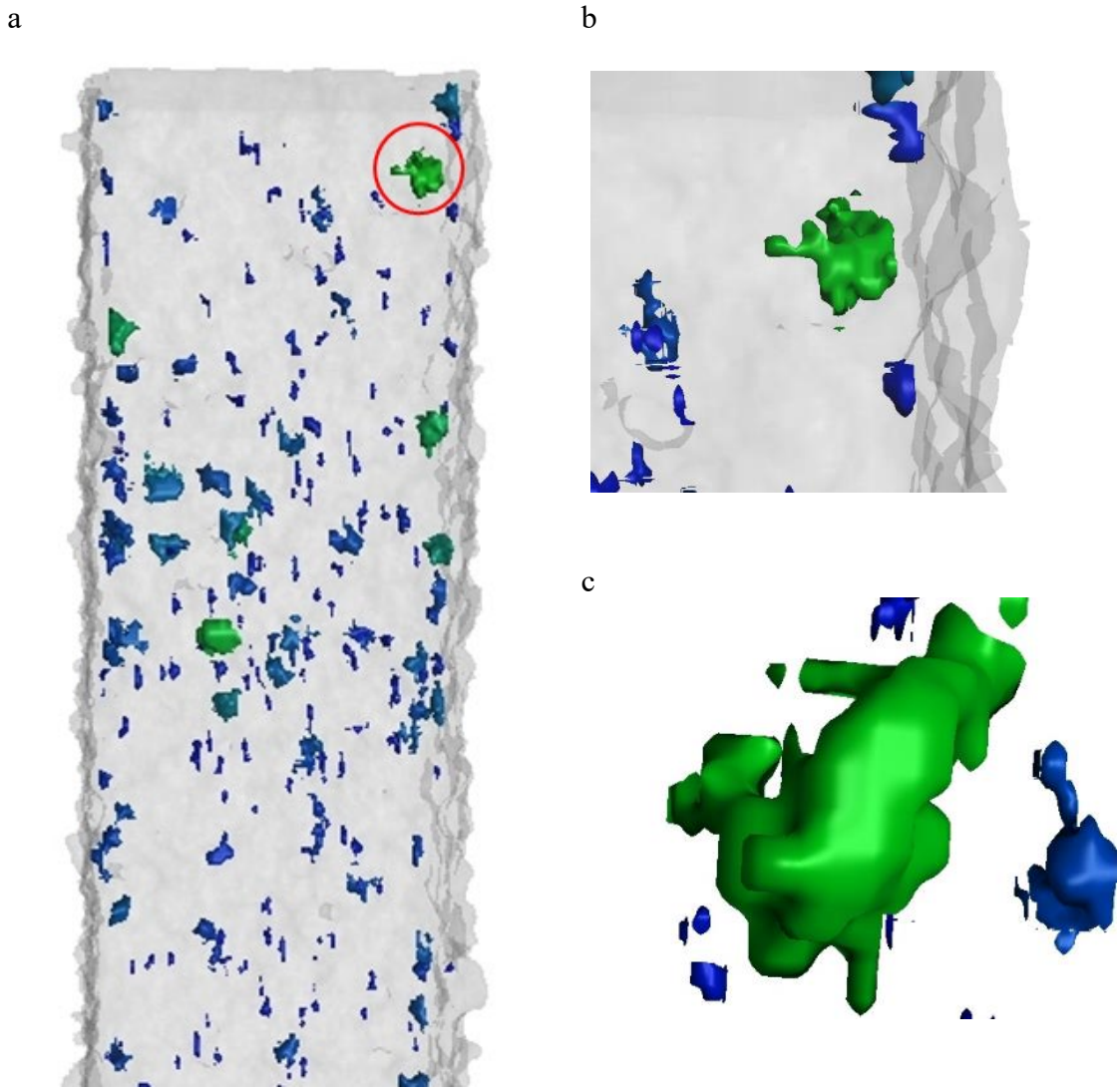

Figure 33. Example of keyhole porosity in high GED sample showing non-spherical shape and distance from center shown at different magnifications.

While low sphericity is not an absolute indicator of keyhole porosity, as keyhole porosity can be shaped anywhere between a sphere and a “keyhole” shape and lack of fusion pores tend to be severely non-spherical, keyhole porosity tends to be less spherical when energy input is too high. Results in this study have been found to be in confirmation of this trend, in which sphericity values decrease as energy density increases, specifically in the highest-volume pores, which are those hypothesized to be keyhole pores.

However, it is important to note that gas porosity, formed by entrapped gas, typically takes on a highly spherical shape. This could be a reason why, as shown in Table 11, porosity values are highest in the smallest pores and lowest in the largest pores. It is hypothesized that the combination of non-spherical keyhole porosity and spherical gas porosity are both contributing to this trend.

Table 11. Sphericity Values by Porosity Volumetric Percentile Range

Percentile Range	High GED	Nominal GED	Low GED
All Pores: 0-100	0.550	0.533	0.555
0-25	0.596	0.578	0.595
25-50	0.579	0.556	0.578
50-75	0.550	0.529	0.548
75-100	0.489	0.466	0.487
90-100	0.466	0.429	0.449
98.5-100	0.468	0.425	0.453

1.13.2 Defect-Property Relationships

Correlation results shown above have significant implications for the use of CT inspection and other non-destructive evaluation methods in the inspection and qualification of additively manufactured 316L SS components. Firstly, it can be concluded that quantitative SEM inspection provided useful data on the relationships between porosity and tensile performance. These results demonstrated that relationships exist between porosity metrics, particularly size and location, and the tensile performance metrics of UTS strain and ductility. However, it should be noted that quantitative SEM inspections are limited due to the nature of inspections occurring post-fracture and therefore not being practical for real inspection applications. Additionally, SEM results are hampered by the necking phenomena occurring during tensile failure, which evolve the porosity characteristics due to deformation. The material used in this study is particularly ductile,

having elongation to failure strains in excess of 70%, in which necking reduction in area is significant. Thus, SEM results are useful for understanding and elucidating the defect-property relationships for AM 316L SS, but not as an inspection tool.

While SEM can provide very high-resolution inspection of fracture surfaces, CT is a non-destructive method and can thus be used prior to commissioning a part for service and is an inspection tool that can be used in real scenarios for component inspection and qualification. The necking phenomena observed in the SEM results does not exist in the CT results, making CT a much better tool for this type of study. The present CT-based results revealed moderate correlation between pore size metrics and tensile performance when considering all pores in an inspection with coefficient of determination values of the strongest relationships around 0.3-0.5. However, upon refinement of porosity assessment by only considering pores > 150 μm in diameter, the coefficient of determination values between porosity metrics and tensile properties were drastically improved and, in some cases, revealed, as in the distance to center porosity metric that improved from a COD value of 0.00 to 0.49 for its relationship with modulus. Additionally, porosity size metrics improved from ~0.5 to up to 0.79. This increase in COD improves the reliability of using porosity descriptors as performance predictors significantly. This increase in prediction reliability means that using CT for porosity inspection could be a feasible inspection method for components subject to tensile loading. The improved correlation results, shown in Figure 31, have two main implications for the qualification of additively manufactured 316L. 1) porosity inspections can be used as predictors of tensile performance and 2) adequate inspections can be performed using relatively low-resolution inspection methods.

Porosity has long been suspected to be detrimental to tensile performance. However, relatively few studies have attempted to quantify its effects with any real success. The results presented in this study indicate that porosity can be used as one metric of part qualification. This is significant for the AM community because the understanding of the relationship between porosity and tensile performance means that parts can begin to be qualified for use without testing many specific components to establish inspection metrics on a component-by-component basis.

Perhaps the most significant impact of the results presented above are that only the largest pores in a sample need to be considered for performance predictions. The feasibility of low-resolution inspection methods for performance predictions means that computed tomography inspections do not need to be research-grade systems because they only need to detect relatively large pores at approximately 150 μm and larger. Additionally, the advantage of only needing to detect large pores means that the probability of detection (POD) significantly increases. This means that the confidence in inspection results of both whether a pore truly exists as well as its characteristics will be very high. Furthermore, it is plausible to think that with only relatively large pores needing to be detected, nondestructive inspection methods other than computed tomography may be adequate. Ultrasonics has potential in this area with adequately low-surface roughness components however, it is likely that radiography will remain the preferred inspection method. The present results indicate that: 1) only large pores need to be detected and 2) shape of porosity is relatively insignificant in impact on performance. Thus, digital radiography (DR), which is the acquisition of two-dimensional x-ray radiographs/projections, may be sufficient for detecting whether pores exist which exceed an inspection threshold. The acquisition of one

or only a few radiographs would drastically decrease the time and cost associated with inspection of parts as compared to CT, which requires hundreds to thousands of radiographs to be taken as well as costly analysis software and highly-skilled and expensive analysts. Decrease in inspection time could decrease from several hours to several minutes if projections could be used for full inspections. At minimum, DR may be adequate as an initial inspection step that could be used to flag components that are near the qualification threshold for more in-depth CT inspection.

Important to the analysis of the results presented in this study is that the samples used were very small, thin components of 1 mm^2 cross-sectional area. With that in mind, one must qualify the conclusions drawn in this section that these trends in defect-property relationships have only been demonstrated for these small components. In these samples, defects were relatively large in comparison to the size of the stressed area. Thus, it is probable that these trends do not continue or are different in parts of larger stressed areas in which the defect-to-stressed-area size ratio is significantly less. However, with the advantages offered by additive manufacturing in terms of part complexity, it will become increasingly common for parts, such as lattice structures, to be printed with very small features comparable in size to samples tested in this study.

Results presented in this study are consistent with other studies such as that by Madison et al. [55] and Kramer et al. [20] in the conclusion that porosity impacts tensile performance of additively manufactured components. Ref. [55], investigating 17-4PH stainless steel, found that maximum COD values of approximately 0.50 exist for correlation of porosity characteristics and tensile performance. These results, despite being performed on a different material system, are very similar to results in this study. The

present study, however, found that consideration of only the largest pores can be significantly improve the COD values of these relationships. Ref. [20], investigating 316L SS, found that voids encourage cracks to initiate grow more quickly and that fracture path was affected by porosity. The early initiation of cracks by large voids is consistent with the low elongation properties seen in the samples of the present study. This study did not investigate the strength of these relationships should COD analysis, but concluded that an obvious relationship between voids and mechanical behavior remained elusive. The similar conclusions of the present study to other studies lends legitimacy to the correlations presented here and provides further understanding of the reasons for low elongation values in samples with large porosity from a fracture mechanics perspective.

CONCLUSIONS AND FUTURE WORK

1.14 Study Overview

The present work was focused on developing an understanding of the role of internal porosity defects created by variations in spatial energy distributions on global tensile performance of 316L SS samples. Currently, there is a significant lack of understanding of this relationship for the broad range of engineering alloys of interest to metal additive manufacturing. This thesis developed an improved understanding of this relationship and is useful for the development of inspection standards critical for critical parts such as those in aerospace and defense.

For this study, tensile samples were manufactured using a laser powder bed fusion system in three different builds at three different energy densities. The samples, attached on a plate to form an array of tensile samples, were inspected using an x-ray computed tomography system. Using this this inspection method, three-dimensional porosity data were extracted. Following tensile testing of the samples using an automated, high-throughput tensile testing system, the resulting fracture surfaces were inspected using scanning electron microscopy. Quantitative techniques were used to extract metrics regarding porosity seen on the fracture surfaces. Using information extracted from both CT and SEM inspections, porosity characteristics were correlated with mechanical properties learned through tensile testing using linear least squares regression.

1.15 Conclusions

Using thorough, quantitative, and comprehensive inspection and analysis techniques, additively manufactured 316L stainless steel global tensile properties were correlated with quantitative porosity descriptors. Correlation matrices such as those in Figure 30 were used to directly identify the strength of relationships between porosity characteristics and intrinsic mechanical properties. By determining the strength of these trends, confidence levels for part inspection can be established based on how well a porosity characteristic is correlated with global tensile behavior. The major conclusions of this study are:

1. The largest pores in a sample have the largest impact on global tensile behavior.
2. Volume is the most significant porosity characteristic, of those investigated, that is correlated with tensile behavior.
3. Ductility and strain at ultimate tensile strength are significantly negatively impacted by porosity.
4. Elastic modulus is minorly affected by porosity.
5. Pore shape has little effect on tensile properties.

The first of these conclusions, that the largest pores have the largest impact on tensile behavior, was shown predominantly through the significant improvement in coefficient of determination values between CT-measured porosity characteristics and mechanical properties when only pores larger than 150 μm in diameter were considered. This conclusion is promising for the development of qualification standards because the largest pores will be the pores with the highest probability of detection. This high POD means that

inspectors will be able to achieve high levels of confidence in their inspection of these parts. Additionally, it opens up the potential of using alternative inspection methods besides CT such as simple DR. CT porosity data compared with tensile behavior demonstrated that volume is the most reliable predictor of the defect-property relationship. High reliability as a predictor is important because it increases confidence in the decision to accept or reject a part. High confidence in inspections will help minimize the number of parts rejected. Additionally, volume is a relatively simple porosity metric that simplifies inspection.

Both ductility and strain at UTS were shown to be negatively impacted by porosity, as measured by volume and other characteristics. This is important because 316L SS is often chosen for its ductile material response. Understanding of the relationship between porosity and performance can help inform decisions when designing a component or selecting a material. Elastic modulus was shown to be fairly constant across all GED conditions and only moderately correlated with porosity characteristics, making it unsuitable for performing inspections. This is consistent with the findings of others and shows that porosity needs relatively little consideration when designing components that will only experience elastic loading conditions. Lastly, little to no correlation was seen between pore shape and global tensile performance. It is suspected that pore shape may have impact on local tensile behavior or under fatigue loading conditions where defect shape often is more significant.

1.16 Contributions

The contributions of this study center around the thoroughness of inspections, number of samples inspected and tested, and the number of relationships analyzed. This thoroughness as well as inspection detail allowed for the accurate assessment of porosity characteristics, particularly those such as size and shape which are heavily influenced by inspection resolution. Specifically, this study investigated the effects of only the largest pores and found that these pores had a dominating effect on global tensile performance. This conclusion contributes to the cumulative knowledge of the effects of porosity on additively manufactured 316L SS. Additionally, this finding can aid in the speed of development of inspection standards as well as their reliability. The usefulness of establishing thresholds allows for inspectors to have confidence that only pores above this threshold need to be detected to predict material properties.

1.17 Limitations

Limitations of this study center around the variety of factors that may have skewed the true relationships between porosity characteristics and measured mechanical properties. Important to interpreting and understanding the work presented in this document is the distinction between correlation and causation. This work presents correlations between porosity characteristics and global mechanical properties, which is valuable for understanding these relationships and predicting performance based on porosity inspections. However, there are many variables influencing mechanical properties besides porosity and thus it is difficult to isolate any one variable as the true cause. These other variables predominantly include microstructure, surface roughness, and surface defects. It

has been shown that variations in energy density can result in different microstructural and surface roughness characteristics. Thus, the direct relationship between porosity, which is controlled via energy density, and mechanical properties cannot be entirely isolated due to the number of variables associated with GED. Consequently, the data presented in this thesis needs to be carefully interpreted so as not to draw conclusions that porosity characteristics are the sole cause or causes of deterioration in global tensile performance.

Other limitations include the resolution attained in CT scans. Due to the discrete nature of CT scans, interpolation must be performed to determine porosity characteristics, and errors associated with this are particularly prevalent in morphological characteristics. Increased resolution would additionally provide information on pores that are below the detection threshold of the current system. However, it is anticipated that these smaller pores would have shown relatively little effect on performance given the conclusions of this study.

1.18 Future Work

Although this document presents results that improve the understanding of the defect-property relationship in AM 316L SS, there is significant work that remains before this relationship is fully understood. One major question in the AM research field is the scalability of defect influence. In other words, do pores have the same relationships shown in this study when part size increases? Additionally, what is the threshold at which pores do not need to be considered for prediction of global mechanical performance? What other factors are influencing mechanical properties that are not being properly removed from experimentation or accounted for in analysis?

In order to more thoroughly understand the role of porosity in mechanical performance, variables such as surface roughness or microstructure variations, both inter- and intra-part, need to be either eliminated or accounted for. An example of such a study involves machining or grinding samples to achieve a uniform desired surface roughness. Furthermore, heat treatments could be performed to normalize microstructure across all samples. These steps would allow for further isolation of porosity as a study's independent variable and provide clearer insight into the relationship between porosity and global mechanical performance.

Overall, there is a significant amount of work that still needs to be performed before qualification standards can be written for AM components. However, this paper provided valuable insight into the defect-property relationship in AM 316L SS through the correlation of porosity found through SEM and CT inspections and tensile testing.

REFERENCES

[1] Yang, L., Hsu, K., Baughman, B., Godfrey, D., Medina, F., Menon, M., and Wiener, S., 2017, *Additive Manufacturing of Metals: The Technology, Materials, Design and Production*, Springer Berlin Heidelberg, New York, NY.

[2] Dressler, A. D., Jost, E. W., Miers, J. C., Moore, D. G., Seepersad, C. C., and Boyce, B. L., 2019, "Heterogeneities Dominate Mechanical Performance of Additively Manufactured Metal Lattice Struts," Additive Manufacturing, **28**, pp. 692–703.

[3] Wauthle, R., Vrancken, B., Beynaerts, B., Jorissen, K., Schrooten, J., Kruth, J.-P., and Van Humbeeck, J., 2015, "Effects of Build Orientation and Heat Treatment on the Microstructure and Mechanical Properties of Selective Laser Melted Ti6al4v Lattice Structures," Additive Manufacturing, **5**, pp. 77–84.

[4] Peacock, G. J., 1903, "Method of Making Composition Horseshoes."

[5] Seifi, M., Salem, A., Beuth, J., Harrysson, O., and Lewandowski, J. J., 2016, "Overview of Materials Qualification Needs for Metal Additive Manufacturing," JOM, **68**(3), pp. 747–764.

[6] Flynn, J. M., Shokrani, A., Newman, S. T., and Dhokia, V., 2016, "Hybrid Additive and Subtractive Machine Tools – Research and Industrial Developments," International Journal of Machine Tools and Manufacture, **101**, pp. 79–101.

[7] Lorenz, K. A., Jones, J. B., Wimpenny, D. I., and Jackson, M. R., "A REVIEW OF HYBRID MANUFACTURING," p. 13.

[8] Hill, L., Sparks, T., and Liou, F., "Development of a Hybrid Manufacturing Process for Precision Metal Parts," p. 17.

[9] Yamazaki, T., 2016, "Development of A Hybrid Multi-Tasking Machine Tool: Integration of Additive Manufacturing Technology with CNC Machining," Procedia CIRP, **42**, pp. 81–86.

[10] Lauwers, B., Klocke, F., Klink, A., Tekkaya, A. E., Neugebauer, R., and Mcintosh, D., 2014, "Hybrid Processes in Manufacturing," CIRP Annals, **63**(2), pp. 561–583.

[11] Osanov, M., and Guest, J. K., 2016, "Topology Optimization for Architected Materials Design," Annual Review of Materials Research, **46**(1), pp. 211–233.

[12] Slotwinski, J. A., and Garboczi, E. J., 2015, "Metrology Needs for Metal Additive Manufacturing Powders," JOM, **67**(3), pp. 538–543.

[13] Kim, F. H., and Moylan, S. P., 2018, *Literature Review of Metal Additive Manufacturing Defects*, NIST AMS 100-16, National Institute of Standards and Technology, Gaithersburg, MD.

[14] Cheng, B., Lydon, J., Cooper, K., Cole, V., Northrop, P., and Chou, K., "Melt Pool Dimension Measurement In Selective Laser Melting Using Thermal Imaging," p. 12.

[15] Spears, T. G., and Gold, S. A., 2016, "In-Process Sensing in Selective Laser Melting (SLM) Additive Manufacturing," Integrating Materials and Manufacturing Innovation, **5**(1).

[16] Leach, R. K., Bourell, D., Carmignato, S., Donmez, A., Senin, N., and Dewulf, W., 2019, "Geometrical Metrology for Metal Additive Manufacturing," CIRP Annals, **68**(2), pp. 677–700.

[17] Seifi, M., Gorelik, M., Waller, J., Hrabe, N., Shamsaei, N., Daniewicz, S., and Lewandowski, J. J., 2017, "Progress Towards Metal Additive Manufacturing Standardization to Support Qualification and Certification," JOM, **69**(3), pp. 439–455.

[18] Seifi, M., Salem, A., Satko, D., Shaffer, J., and Lewandowski, J. J., 2017, "Defect Distribution and Microstructure Heterogeneity Effects on Fracture Resistance and Fatigue Behavior of EBM Ti–6Al–4V," International Journal of Fatigue, **94**, pp. 263–287.

[19] Boyce, B. L., Salzbrenner, B. C., Rodelas, J. M., Swiler, L. P., Madison, J. D., Jared, B. H., and Shen, Y.-L., 2017, "Extreme-Value Statistics Reveal Rare Failure-Critical Defects in Additive Manufacturing: Extreme-Value Statistics Reveal Rare Failure-Critical Defects…," Advanced Engineering Materials, **19**(8), p. 1700102.

[20] Kramer, S. L. B., Ivanoff, T. A., Madison, J. D., and Lentfer, A. P., 2019, "Evolution of Damage and Failure in an Additively Manufactured 316l Ss Structure: Experimental Reinvestigation of the Third Sandia Fracture Challenge," Int J Fract.

[21] Carlton, H. D., Klein, K. D., and Elmer, J. W., 2019, "Evolution of Microstructure and Mechanical Properties of Selective Laser Melted Ti-5Al-5V-5Mo-3Cr after Heat Treatments," Science and Technology of Welding and Joining, pp. 1–9.

[22] Roach, R. A., Abdeljawad, F., Argibay, N., Allen, K., Balch, D., Beghini, L., Bishop, J., Boyce, B., Brown, J., Burchard, R., Chandross, M., Cook, A., Dressler, A., Forrest, E., Ford, K., Ivanoff, T., Jared, B., Kammler, D., Koepke, J., Kustas, A., Lavin, J., Leathe, N., Lester, B., Madison, J., Mani, S., Martinez, M. J., Moser, D., Murphy, R., Rodgers, T., Seidl, T., Shaklee-Brown, H., Stanford, J., Stender, M., Sugar, J., Swiler, L. P., Taylor, S., Trembacki, B., Waanders, B. van B., Whetton, S., Wildey, T., and Wilson, M., "Born Qualified Grand Challenge LDRD Final Report," p. 105.

[23] Peralta, A. D., Enright, M., Megahed, M., Gong, J., Roybal, M., and Craig, J., 2016, "Towards Rapid Qualification of Powder-Bed Laser Additively Manufactured Parts," Integrating Materials and Manufacturing Innovation, **5**(1).

[24] Roach, R. A., Bishop, J. E., Johnson, K., Rodgers, T., Boyce, B. L., and Swiler, L., "Using Additive Manufacturing as a Pathway to Change the Qualification Paradigm," p. 11.

[25] Maire, E., and Withers, P. J., 2014, "Quantitative X-Ray Tomography," International Materials Reviews, **59**(1), pp. 1–43.

[26] Kim, F. H., Moylan, S. P., Garboczi, E. J., and Slotwinski, J. A., 2017, "Investigation of Pore Structure in Cobalt Chrome Additively Manufactured Parts Using X-Ray Computed Tomography and Three-Dimensional Image Analysis," Additive Manufacturing, **17**, pp. 23–38.

[27] DebRoy, T., Wei, H. L., Zuback, J. S., Mukherjee, T., Elmer, J. W., Milewski, J. O., Beese, A. M., Wilson-Heid, A., De, A., and Zhang, W., 2018, "Additive Manufacturing

of Metallic Components – Process, Structure and Properties," Progress in Materials Science, **92**, pp. 112–224.

[28] Martin, A. A., Calta, N. P., Khairallah, S. A., Wang, J., Depond, P. J., Fong, A. Y., Thampy, V., Guss, G. M., Kiss, A. M., Stone, K. H., Tassone, C. J., Nelson Weker, J., Toney, M. F., van Buuren, T., and Matthews, M. J., 2019, "Dynamics of Pore Formation During Laser Powder Bed Fusion Additive Manufacturing," Nat Commun, **10**(1), p. 1987.

[29] Madison, J. D., and Aagesen, L. K., 2012, "Quantitative Characterization of Porosity in Laser Welds of Stainless Steel," Scripta Materialia, **67**(9), pp. 783–786.

[30] King, W. E., 2014, "Observation of Keyhole-Mode Laser Melting in Laser Powder-Bed Fusion Additive Manufacturing," Journal of Materials Processing Technology, p. 11.

[31] Alberts, D., Schwarze, D., and Witt, G., "In Situ Melt Pool Monitoring and the Correlation to Part Density of Inconel® 718 for Quality Assurance in Selective Laser Melting," p. 14.

[32] Aminzadeh, M., and Kurfess, T. R., 2018, "Online Quality Inspection Using Bayesian Classification in Powder-Bed Additive Manufacturing from High-Resolution Visual Camera Images," Journal of Intelligent Manufacturing.

[33] Chivel, Y., 2013, "Optical In-Process Temperature Monitoring of Selective Laser Melting," Physics Procedia, **41**, pp. 904–910.

[34 Chivel, Yu., and Smurov, I., 2010, "On-Line Temperature Monitoring in Selective Laser Sintering/Melting," Physics Procedia, **5**, pp. 515–521.

[35] Craeghs, T., Bechmann, F., Berumen, S., and Kruth, J.-P., 2010, "Feedback Control of Layerwise Laser Melting Using Optical Sensors," Physics Procedia, **5**, pp. 505–514.

[36] Grasso, M., Laguzza, V., Semeraro, Q., and Colosimo, B. M., 2016, "In-Process Monitoring of Selective Laser Melting: Spatial Detection of Defects Via Image Data Analysis," Journal of Manufacturing Science and Engineering, **139**(5), p. 051001.

[37] Lane, B., Moylan, S., Whitenton, E. P., and Ma, L., 2016, "Thermographic Measurements of the Commercial Laser Powder Bed Fusion Process at NIST," Rapid Prototyping Journal, **22**(5), pp. 778–787.

[38] Moylan, S., Whitenton, E., Lane, B., and Slotwinski, J., 2014, "Infrared Thermography for Laser-Based Powder Bed Fusion Additive Manufacturing Processes," Baltimore, Maryland, USA, pp. 1191–1196.

[39] Tapia, G., and Elwany, A., 2014, "A Review on Process Monitoring and Control in Metal-Based Additive Manufacturing," Journal of Manufacturing Science and Engineering, **136**(6), p. 060801.

[40] Lane, B., Grantham, S., Yeung, H., Zarobila, C., and Fox, J., "Performance Characterization of Process Monitoring Sensors on the Nist Additive Manufacturing Metrology Testbed," p. 10.

[41 Wycisk, E., Solbach, A., Siddique, S., Herzog, D., Walther, F., and Emmelmann, C., 2014, “Effects of Defects in Laser Additive Manufactured Ti-6Al-4V on Fatigue Properties,” Physics Procedia, **56**, pp. 371–378.

[42] Chastand, V., Tezenas, A., Cadoret, Y., Quaegebeur, P., Maia, W., and Charkaluk, E., 2016, “Fatigue Characterization of Titanium Ti-6Al-4V Samples Produced by Additive Manufacturing,” Procedia Structural Integrity, **2**, pp. 3168–3176.

[43] Günther, J., Krewerth, D., Lippmann, T., Leuders, S., Tröster, T., Weidner, A., Biermann, H., and Niendorf, T., 2017, “Fatigue Life of Additively Manufactured Ti–6Al–4V in the Very High Cycle Fatigue Regime,” International Journal of Fatigue, **94**, pp. 236–245.

[44] Greitemeier, D., Palm, F., Syassen, F., and Melz, T., 2017, “Fatigue Performance of Additive Manufactured Tial6v4 Using Electron and Laser Beam Melting,” International Journal of Fatigue, **94**, pp. 211–217.

[45] Leuders, S., Vollmer, M., Brenne, F., Tröster, T., and Niendorf, T., 2015, “Fatigue Strength Prediction for Titanium Alloy TiAl6V4 Manufactured by Selective Laser Melting,” Metallurgical and Materials Transactions A, **46**(9), pp. 3816–3823.

[46] Leuders, S., Thöne, M., Riemer, A., Niendorf, T., Tröster, T., Richard, H. A., and Maier, H. J., 2013, “On the Mechanical Behaviour of Titanium Alloy Tial6v4 Manufactured by Selective Laser Melting: Fatigue Resistance and Crack Growth Performance,” International Journal of Fatigue, **48**, pp. 300–307.

[47] Liu, Q. C., Elambasseril, J., Sun, S. J., Leary, M., Brandt, M., and Sharp, P. K., 2014, "The Effect of Manufacturing Defects on the Fatigue Behaviour of Ti-6Al-4V Specimens Fabricated Using Selective Laser Melting," Advanced Materials Research, **891–892**, pp. 1519–1524.

[48] Brandl, E., Heckenberger, U., Holzinger, V., and Buchbinder, D., 2012, "Additive Manufactured AlSi10Mg Samples Using Selective Laser Melting (SLM): Microstructure, High Cycle Fatigue, and Fracture Behavior," Materials & Design, **34**, pp. 159–169.

[49] Uzan, N. E., Shneck, R., Yeheskel, O., and Frage, N., 2017, "Fatigue of Alsi10mg Specimens Fabricated by Additive Manufacturing Selective Laser Melting (Am-Slm)," Materials Science and Engineering: A, **704**, pp. 229–237.

[50] Romano, S., Brückner-Foit, A., Brandão, A., Gumpinger, J., Ghidini, T., and Beretta, S., 2018, "Fatigue Properties of Alsi10mg Obtained by Additive Manufacturing: Defect-Based Modelling and Prediction of Fatigue Strength," Engineering Fracture Mechanics, **187**, pp. 165–189.

[51] Zhang, H., Toda, H., Qu, P. C., Sakaguchi, Y., Kobayashi, M., Uesugi, K., and Suzuki, Y., 2009, "Three-Dimensional Fatigue Crack Growth Behavior in an Aluminum Alloy Investigated with in Situ High-Resolution Synchrotron X-Ray Microtomography," Acta Materialia, **57**(11), pp. 3287–3300.

[52] Huynh, L., Rotella, J., and Sangid, M. D., 2016, "Fatigue Behavior of In718 Microtrusses Produced Via Additive Manufacturing," Materials & Design, **105**, pp. 278–289.

[53] Sheridan, L., Scott-Emuakpor, O. E., George, T., and Gockel, J. E., 2018, "Relating Porosity to Fatigue Failure in Additively Manufactured Alloy 718," Materials Science and Engineering: A, **727**, pp. 170–176.

[54] Riemer, A., Leuders, S., Thöne, M., Richard, H. A., Tröster, T., and Niendorf, T., 2014, "On the Fatigue Crack Growth Behavior in 316L Stainless Steel Manufactured by Selective Laser Melting," Engineering Fracture Mechanics, **120**, pp. 15–25.

[55] Madison, J. D., Underwood, O. D., Swiler, L. P., Boyce, B. L., Jared, B. H., Rodelas, J. M., and Salzbrenner, B. C., 2018, "Corroborating Tomographic Defect Metrics with Mechanical Response in an Additively Manufactured Precipitation-Hardened Stainless Steel," Provo, Utah, USA, p. 020009.

[56] Carlton, H. D., Haboub, A., Gallegos, G. F., Parkinson, D. Y., and MacDowell, A. A., 2016, "Damage Evolution and Failure Mechanisms in Additively Manufactured Stainless Steel," Materials Science and Engineering: A, **651**, pp. 406–414.

[57] Torres-Sanchez, C., McLaughlin, J., and Bonallo, R., 2018, "Effect of Pore Size, Morphology and Orientation on the Bulk Stiffness of a Porous Ti35Nb4Sn Alloy," Journal of Materials Engineering and Performance, **27**(6), pp. 2899–2909.

[58] Miers, J. C., Jost, E. W., Moore, D. G., Jared, B., and Salanda, C., 2019, “Effects of Pore Orientation and Shape on Failure in Additively Manufactured 316L SS,” Garden Grove, CA.

[59] Gong, H., Rafi, K., Gu, H., Janaki Ram, G. D., Starr, T., and Stucker, B., 2015, “Influence of Defects on Mechanical Properties of Ti–6al–4v Components Produced by Selective Laser Melting and Electron Beam Melting,” Materials & Design, **86**, pp. 545–554.

[60] Salzbrenner, B. C., Rodelas, J. M., Madison, J. D., Jared, B. H., Swiler, L. P., Shen, Y.-L., and Boyce, B. L., 2017, “High-Throughput Stochastic Tensile Performance of Additively Manufactured Stainless Steel,” Journal of Materials Processing Technology, **241**, pp. 1–12.